University of Wisconsin Milwaukee

UWM Digital Commons

August 2021

Bonding Evaluation of Graphene-Oxide Layers on Flexible Substrates

Maysam Rezaee
University of Wisconsin-Milwaukee

BONDING EVALUATION OF GRAPHENE-OXIDE

LAYERS ON FLEXIBLE SUBSTRATES

by

Maysam Rezaee

A Dissertation Submitted in

Partial Fulfillment of the

Requirements for the Degree of

Doctor of Philosophy

in Engineering

at

The University of Wisconsin-Milwaukee

August 2021

ABSTRACT

BONDING EVALUATION OF GRAPHENE-OXIDE LAYERS ON FLEXIBLE
SUBSTRATES

by

Maysam Rezaee

The University of Wisconsin-Milwaukee, 2021
Under the Supervision of Professor Nathan P. Salowitz

Flexible electronics are getting interest in development of field effects transducers such as biomedical health screening tools, structural health monitoring in infrastructures, aerospace, vehicular industries and cell phones. As a promising candidate for flexible electronics, graphene-based devices have been developed through exceptional electrochemical and thermomechanical properties of graphene. Reducing the graphene oxide enables creation of large scale devices through its high manufacturability.

Same as other types of electronics, the bonding of sensing units to the substrate is significantly dependent to the deposition method used for the fabrication of device. In this study, the mechanical strength of reduced graphene oxide (rGO) layers on the polymeric substrates is evaluated while the rGO layers are deposited by drop casting on the substrate. The tape test is adopted to measure the failure strength at the interface of rGO layers and substrate. To achieve a consistent and repeatable measurement of peel force, a new design of peel test fixture is suggested to control effective parameters on the peel test and keep constant the peel rate and angle. The new design of peel test has shown low coefficient of variation of about 8% for peel force measurement, which is much lower than 37% reported by ASTM

standard for the tape test. Employing an image processing technique, a geometric analysis is conducted to identify the contributions of cohesive and adhesive failures in overall peel force. A mathematical method is developed to connect the geometric analysis result from the image processing to the experimental peel force measure. As a result of mathematical method, the magnitude of cohesive and adhesive energies are identified. Performing analysis of variation (ANOVA) on the bonding energies, the significant parameters of thermal processing on the bonding strength of rGO layers and substrates are determined so that the concentration of GO solution has illustrated as the most significant factor. The surface treatment duration for GO and substrates are the next priorities of significant factors.

In this study, the mechanical strength and performance of rGO-based electronics were evaluated based on a new methodology for the peel test. The Kapton has demonstrated the best performance and is served as the best candidate for the fabricating of rGO-based electronics based on thermal processing. The PDMS showed high potential for being a suitable candidate for graphene-based electronics. Considering low surface energy of Teflon (PTFE), it would be viable candidate for transfer printing of graphene-based sensors. Despite the rGO layers showed very low adhesion boding to the Teflon substrate, the rGO layers on the Teflon had shown good uniformity itself.

TABLE OF CONTENTS

LIST OF FIGURES

LIST OF TABLES

ACKNOWLEDGEMENTS

Chapter 1: Introduction

1.1 Motivation

Flexible micro/nano-fabricated electronics are seeing significant interest recently because of their applicability in diverse fields like wearable sensors on skin, implantable sensors, and structural health monitoring. They are expected to be foldable and rollable during extreme events and survive large deformation in bending or elongation etc. Microfabricated devices are usually made by deposition of thin films (as the electronics) on a substrate using various methods including sputter coating,[1] atomic layer deposition,[2] e-beam evaporation,[3] or drop casting,[4,5] . The interlayer bonding of films (or flakes) and interface bonding between films and substrate are critical to the mechanical strength of microfabricated devices. The mechanical, electrical, and chemical properties of graphene,[6–13] make it is a strong candidate for fabricating new generation of electronics.[14–16] Sharing many properties of graphene, reduced Graphene Oxide (rGO) can be used with more straightforward synthesis processes that enable fabrication of large-scale graphene-based devices.[14,16–19]

In spite of significant complex and expensive research done on the bonding evaluation of mono/multi-layer graphene flakes on rigid/flexible substrates,[20–29] the bonding of rGO layers has received minimal attention to date.

1.2 Background

Recent technologies are increasingly demanding small-scale devices because of their applicability in the vast areas like field effects transducers (FETs), actuators, and

1

microprocessors. These devices have been fabricated by depositing and/or etching of layers of micro/nano-scale thick materials on rigid or flexible substrates. Depending on the application of these devices, they should survive possible physical loads and abuses like folding, dropping, shipping, scratching, exposure to high temperature and high moisture. Therefore, the mechanical robustness of modern small-scale electronics plays important role on the performance and reliability of these devices.

Boding of thin films has been investigated through many methods in two categories of qualitative and quantitative methods. Many traditional methods offer an imprecise, expensive, and/or complicated method to assess the bonding of thin films.

1.2.1   Peel test

The most common method for evaluation of bonding strength between a thin film and backing is the 'peel test' that might be called 'tape test' when a tape was used in at least one side of test specimen. This test can be done in an arbitrary angle of peeling so that the 90-degree[30,31] and 180-degree peel tests are the most common ones[32,33]. ASTM D3359[34] specifies a qualitative method to assess the bonding strength for macro/micro-scale specimens. ASTM D3359 prescribes creating special cut patterns on a coated surface then manual application and peeling of tape from the cut region. The amount of peeled region is visually assessed and ranked to identify the quality of bonding. This method is cheap and simple, but there are some limitations:

- Manual application of the tape is poorly controlled, with no specified or control of pressure (which is a source of variation in adhesion force as discussed in Chapter 2).

2

- The specified timing of the test after tape application can cause significant variation of peel force (as discussed in Chapter 2.

- The manual application of peel force degrades the accuracy of this method since there is no control on the peel rate or angle, (the most significant factor on the peel force as elaborated in Chapter 2).

- No quantitative recommendation was provided for this method.

- ASTM D3359 recommended a specific tape, which is no longer available.

- ASTM D3359 reported variations of 37% and 70% for within-laboratories and between-laboratories, respectively.

1.2.2 Pull-off test

One of the other most common tests is the pull-off test which is applied mostly in bonding evaluation of paint and metal coating on relatively rigid surfaces like concrete, steel, and wood. This method was standardized by ASTM D-4541[35] and D-7234[36], DIN EN ISO 4624[37] which is recommended for macro-scale bonding tests. The pull-off test is done quantitatively in most of cases such that provides the traction strength at interface of coating layers and rigid substrates. To perform the pull-off test, special dollies are attached to the coating layer (or nano-fabricated layer) with a strong glue and pulled off through mechanical testing machines. Depending on amount of detached coating layer, the bonding strength may be reported by the overall bonding force or interfacial stress.

1.2.3 Shear lap test

To characterize the shear strength of adhesion layers, the shear lap test was created and described in ASTM D-1002[38], D—316301[39], and D-5868-01[40] for macro/micro-scale applications. A universal testing machine is used to pull two initially bonded rigid substrates in opposite directions, placing the lap joint in shear. The forces measured during the tests are used to calculate the shear strength of bonding layer. The shear modulus of substrates is of importance[41] in this test such that makes it inappropriate for flexible substrates.

1.2.4 Bending test

There are two common types of three-point and four-point bending tests that are normally used for bonding evaluation of composite members. In contrast with three-point bending test, the four-point bending tests provides a region with constant bending moment in addition to lower bearing stress applied on samples. ASTM D-1624-05[42] and D-7249[43] to assess the transverse shear of adhesive layers in a quantitative way specified these methods. These tests are conducted through application of symmetric point loads, which is one and two loads for three-point and four-point tests respectively, on a simply supported sample. The simplicity of identification of maximum bending moment and shear force enables to measure the interfacial strength of the coating layer.

1.2.5 Scribe (or Scratch test)

The scribe (or scratch[44]) test is conducted using a stylus tip to apply the normal force in the coating layer and generate parallel lines or patterns. Based on ASTM B-571-97[45], the bonding inadequacy will be obtained after observing broken (or deboned) coating layer

between lines. Although, the scribe test would be affected many factors like the coating mechanical properties, loading rate, and the test speed, this qualitative method is applicable for bonding performance of brittle layers in macro/micro/nano-scale[46,47].

1.2.6   Blister test

The blister test quantifies the bonding of thin films through applying the outward pressure. These tests utilized complex and expensive setup and would be sophisticated for cases with ductile thin films[48]. By this method, the bonding energy based on a combination of membrane theory and fracture mechanics.[48–50]. In blister test, the adhesive energy of thin films is identified based on application of an upward negative pressure to thin film.

1.2.7   Micro/nano indentation test

Obtaining the delamination strength from interfacial fracture of thin film, the micro/nano indentation tests determine the hardness and moduli of thin films[48,51]. This test was specified by ISO 14577-1[52] for micro/micro/nano-scale by defining multi-level indentation force that would be applicable metallic and non-metallic coating. The indentation force is applied using a standard tip in which the shape of indenter tip is a significant factor for nano-scale tests[53].

1.3 Objective Statement

While many tests have been created, they require complex equipment and analysis that creates an indirect evaluation of the strength of thin film materials and bonding. Therefore, the objective of this work is quantification of the mechanical strength of micro/nano-fabricated layers using a simple, cheap, reliable, and repeatable methodology. The

experimental results and the analytical model are connected through a mathematical analysis to evaluate the bonding characteristics of deposited layers of reduced graphene oxide on flexible substrates. The mathematical analysis contains an image processing core which analyzes the failure modes geometrically. This method was then applied to a variety of reduced graphene oxide specimens deposited on different flexible backings that underwent different processing to evaluate which processing produced the strongest adhesion.

Chapter 2: Approach

To evaluate the bonding strength of rGO layers on flexible substrates, a controlled peel test was created based on ASTM 3359-09 (aka "The Tape Test") in which the peel rate and peel angle were kinematically controlled at specified values through a novel deign of the peel test fixture as shown in Figure 2-1. Having controlled the kinematics of the process, a further study was performed to evaluate other factors and their effects on consistency of the results.

Employing factorial design, the significance of application pressure and its duration, and waiting time were demonstrated and imposed on the final form of the test to minimize variation. The novel peel tests were conducted on thermally reduced rGO samples on flexible polymeric substrates to evaluate the mechanical robustness of rGO-based samples. The thermal reduction processing factors like surface treatment, GO concentration, and sonication time were demonstrated as significant factors on mechanical robustness of rGO layers that are presented in this chapter. An image processing technique was used to analyze the how and where rGO particles detached from the substrate. The results given from peel test and image processing are utilized in a mathematical analysis to characterize the bonding failure modes of rGO flakes along each sample.
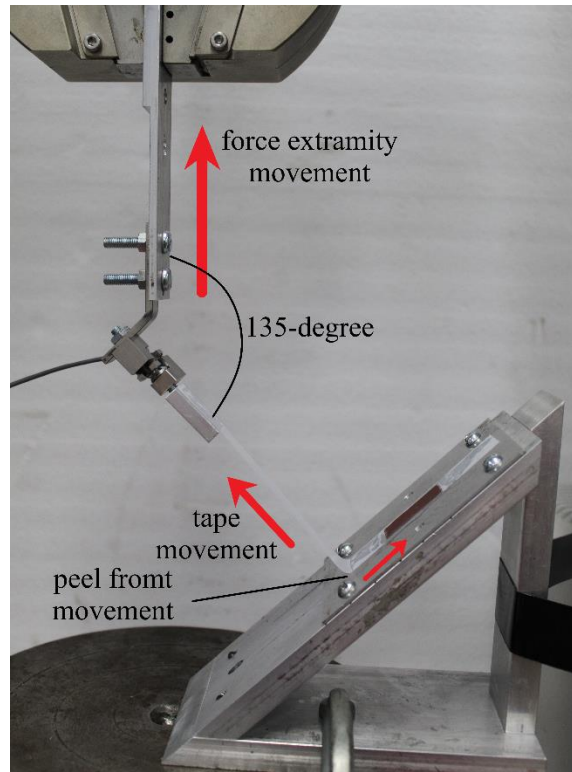
Figure 2-1: suggested peel test design

2.1 Peel Test Mechanics Introduction

Through the simplicity of implementation for quantification of the interface strength of films and solids[30][54–56], the peel test is of the most convenient methods for the measurement the interface tractions. In spite of simple geometry of peel mechanics in macro-scale, there are several reason to take the peel mechanics as a complex problem such as complex mechanical behavior of adhesive layer (or adhesion interface), nonlinear film profile, and viscoelasticity adhesion layer [57–62]. The high complexity of interactions between film and substrate comes from its dependency to the material properties of the adhesive and adherents, peel front rate, and peel angle. Clearly, the identification of stress and strain fields would be sophisticated because they are dependent on the normal deflection of film. Moreover, stresses

8

can be time-dependent for exceedingly small peel rates[63–66]. Despite many mechanical models have been provided to identify the film's configuration (and stress fields), there is no model approved as a reference model that covers peel mechanics appropriately [63,67–73].

The film configuration and variation of interface tractions are highly dependent to the elasticity and viscoelasticity of the adhesive layer in the region of crack propagation [30,63,65,74–76]. The cohesive zone (CZ) models have been developed to model the interface tractions based the film configuration and adhesive layer properties. Considering the vast area of application, such as nano-fabricated electronics [77,78], multi-layers composite structures [79,80], and asphalt mixtures [81–83], the CZ models are being of huge interest to predict the crack path and interfacial strength. These models are presented as Traction-Separation (T-S) models such that they connect the interface traction, t, to the separation displacement, δ, for any point in the fracture zone [84]. Two important parameter for all CZ models are maximum separation displacement, Δ, and the fracture strength, T [85]. The CZ models are distinguished depending on how these two parameters are related.

Dugdale (1960) suggested the constant T-S model [84], shown in Figure 2-2(a), that assumes a constant interface traction for each point up to failure of adhesive layer. Through ease of implementation and good agreement with experimental results [63,69,85,86], the constant T-S model is employed for this study. Increasing the complexity of T-S model, the bilinear T-S model is suggested and examined with many studies, which discretizes the T-S model to pre-crack and post-crack segments (Figure 2-2(b)). The bilinear T-S models provides a reduced compliance of adhesive layer because a roughly stiff connection is established across the pre-crack segment [87–90]. The trapezoidal and power law T-S models are shown in Figure

9

2-2 (c and d) providing more complex traction relations based on separation displacement of adhesive layer among cohesive zone. [91–93]
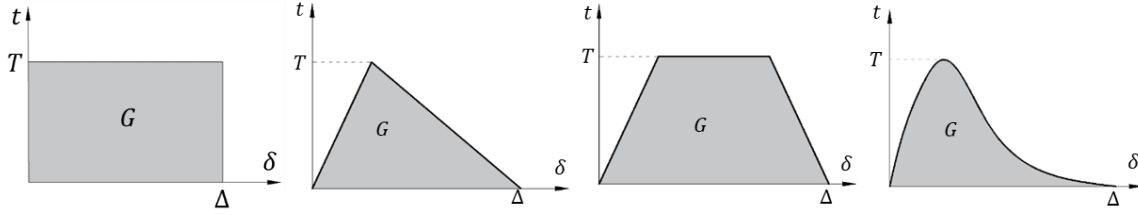
Figure 2-2: CZ models; (a) constant T-S model, (b) bilinear T-S model, (c) trapezoidal T-S model, and (d) power law T-S model

The characteristic of each model is the interface toughness, G, which defines based the fracture strength, T, and maximum separation displacement, Δ as presented in Equation (1). Therefore, for the constant T-S model, the interface toughness is determined as $G = T\Delta$ which corresponds to one of the most theoretical models provided by Kendall (1973) expressing the steady state peel force as the interface toughness for a 90° peel test.[94]

$$G = \int_0^{\Delta} t \, d\delta \qquad\qquad (1)$$

Identification of the peel force requires to determine the film configuration. The peel force variation is tied to variation of CZ length ℓ_c. Apparently, the peel force varies nonlinearly with CZ length up to a steady state. Then, the CZ length reaches out to the L_c, which is defined as steady sate CZ length. This work presents a semi-nonlinear model for the peel test based on constant T-S model to characterize the CZ for cases in which peel force and mechanical properties of film are pre-defined. This method would be applied to identify the CZ properties at the interface of micro/nano-fabricated layers while being assessed by tape test.

10

2.1.1 Theories

Linear bending theory for the peel test

The simplifying assumptions of small deflection and linear elastic behavior of the film, encouraged many researchers to utilize the linear bending theory to analyze the peel test [71,72]. Therefore, it is easy to alter the adhesive layer with an elastic foundation since the interfacial tractions are proportional to the deflection [73]. Mostly, these models were required to assign an initial thickness, t_c, to the adhesive layer same as the model developed by Bikerman (1957) based on a constant T-S CZ model [71]. Therefore, solving the differential equation of $d^4y/dx^4 = -(E_1by)/(EIt_c)$, in which the y is the deflection, E_1 and E are elastic modulus of adhesive layer and film respectively, and b is the width of the film cross-section, the following equation represents the solution of the above differential equation:

$$y = \frac{2nt_cF}{E_1t_c}e^{-nx}\cos nx \tag{2}$$

$$n = \sqrt[4]{3E_1/Et_f^2t_c} \tag{3}$$

where the F is the peel force applied in an angle of 90°. Then, the steady state peel force was obtained as $F_s = 0.3799bS_T\left[(E/E_1)t_ct_f^3\right]^{0.25}$, in which the S_T is the tensile strength of film. As another simplification, the stress concentration at the edges of the thin film was neglected in this model by virtue of elastic behavior of adhesive layer. Introducing the eccentricity of the peel force, Jouwersma (1960) improved the Bikerman model by adding a modification factor on the peel force given from Bikerman model such that $F_{s,jouwersm} = F_{S,Bikerman}/(1 + n_je_c)$ [72]. The parameter e_c is the peel loads eccentricity with respect to the point associated

11

with displacement Δ and $n_j = 1.316\left[(E/E_1)t_c t_f^3\right]^{0.25}$ is a constant value. Yurenka (1962) suggested as almost similar model for thin films on metal substrates [73]. Since a highly nonlinear displacement of the film is anticipated beyond the CZ, the linear bending theory was mostly employed to analyze the film configuration in the CZ[85].

2.1.2 Application of nonlinear elastic bending theory

Regarding to the peel angle and the film configuration, the peel force eccentricity may change the contribution of the fracture modes during the crack propagation. Therefore, a nonlinear model is required to determine the film configuration based on large deformation considerations and anticipated high variation of rotation angle of the film starting from the endpoint of CZ to the peel force extremity.

starting with nonlinear bending theory, the curvature of the film is expressed by $1/\rho = d\theta/ds$ in which the θ is the rotation angle of the film with respect to the *x*-axis and *s* represents the curvilinear coordinate of any point of the film as shown in Figure 2-3-a. Few studies suggested a deformation of an elastica undergoing the nonlinear bending, such as Kaelble (1960), Kendal (1970), and Gent (1975) [55,56,68], considering the following assumptions:

- Elastic deformation

- Semi-infinite length of the film

- Slender rectangular cross-section

The differential equation (4) is fundamental equation of curvature of the film considering the geometric nonlinearity:

$$\frac{1}{\rho} = \frac{\frac{d^2y}{dx^2}}{\left[1 + \left(\frac{dy}{dx}\right)^2\right]^{3/2}} = \frac{Fx}{EI} \qquad (4)$$

Solving the differential equation (4) leads to the film configuration (y) and sequentially the interfacial stress distribution along the CZ [55,95,96]. The solution is applicable for peel angles from zero to 180 degree [56,95].

In this study, the linear bending theory is utilized for the CZ to reduce the complexity of problem in the presence of adhesive layer and identify the film configuration in the CZ. Beyond the CZ, in the fracture zone, the nonlinear bending theory is employed to introduce the peel force eccentricity into the model and determine the film configuration. Since the focus of this work is on the 90-degree peel test, all analyses are done for peel angle of 90 degree.

Semi-Nonlinear elastic bending theory for the peel test

To start with the semi-nonlinear bending theory for the peel test used in this study, the following important assumptions are considered:

- The constant CZ model is employed in which the interface traction is proportional to separation displacement.

- The plane strain state is assumed for the film. Then, $E'=E/(1-v^2)$ and the v is the Poisson's ratio of the film's material.

- As confirmed by many studies, the deformation of the film in the CZ is assumed to follow the small deflection requirements that enables us to use linear bending theory in the CZ [85].

Then, the equation (4) can be reduced to the following form:

13

$$\frac{1}{\rho} = \frac{\frac{d^2y}{dx^2}}{\left[1 + \left(\frac{dy}{dx}\right)^2\right]^{3/2}} \approx \frac{d^2y}{dx^2} = \frac{M}{E'I} \qquad (5)$$
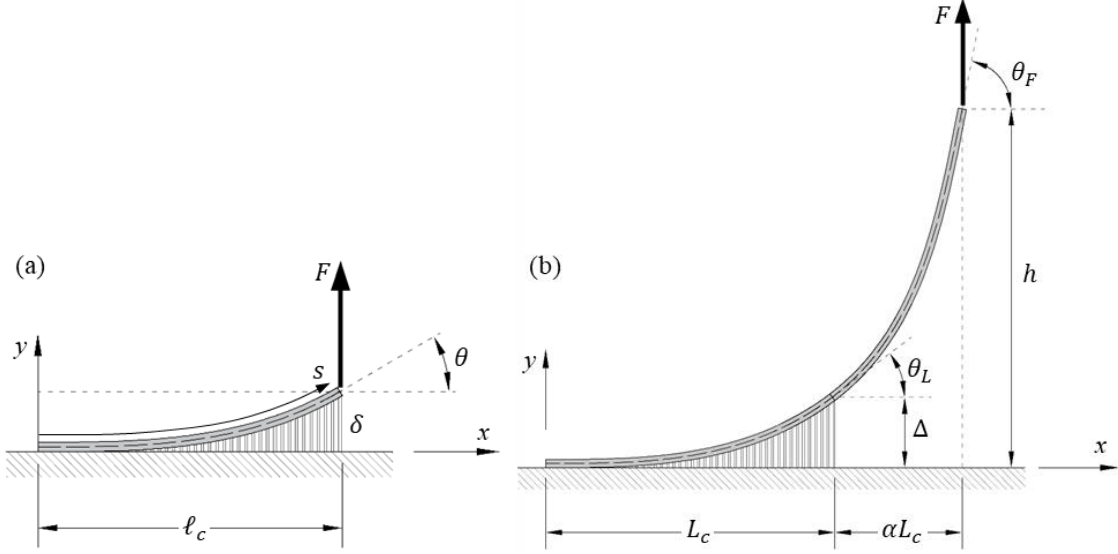
Figure 2-3: Representation of the film geometry (a) in the CZ and (b) beyond the CZ

where the bending moment of a point on the film with horizontal coordinate of x is defined as M. To determine the bending moment using equation (6) it is necessary to know the cohesive zone length (ℓ_c), the interface strength (T), and the peel force (F). This equation is valid before onset steady state peeling, which is equivalent to the steady state CZ length (L_c) and maximum separation displacement (Δ) as shown in Figure 2-3.

$$M = F(\ell_c - x) - \frac{T}{2}(\ell_c - x)^2 \qquad 0 \le x \le L_c \qquad (6)$$

Applying the boundary condition of $M=0$ at $x=0$ for equation (6), when the separation displacement at the end of the CZ meets the value of Δ, the peel force is determined as equation (7):

$$F = \frac{T\ell_c}{2} \qquad (7)$$

14

The nonlinear bending considerations is required right after onset of fracture in the adhesive layer, which is corresponding to first appearance of separation displacement of Δ in the CZ. Beyond this point, the x coordinate of peel force position passes the steady state CZ length, $x>L_c$, and the large displacement of the film pops up through huge variation of the film rotation angle from θ_L to θ_F (as shown in Figure 2-3-b). In this study, the θ_F is set to 90 as the final peel angle is 90 degrees. Then, bending moment and peel force are determined by equations (8) and (9).

$$M = \begin{cases} F(L_c(1+\alpha) - x) - \frac{T}{2}(L_c - x)^2 \\ F(L_c(1+\alpha) - x) \end{cases} \text{ for } \begin{array}{l} 0 \leq x \leq L_c \\ L_c < x < L_c(1+\alpha) \end{array} \tag{8}$$

$$F = \frac{TL_c}{2(1+\alpha)} \tag{9}$$

Employing equations (8) and (9), and applying boundary conditions of $y(0) = 0$ and $y'(0) = 0$, the differential equation of film bending along the CZ (equation (5)) is solved as follows [85]:

$$y(x) = \frac{1+2\alpha}{12(1+\alpha)E'I}TL_c x^3 - \frac{1}{24E'I}Tx^4 \tag{10}$$

The equation (10) indicates the configuration of the film in the CZ after onset of the adhesive layer fracture. To identify the film configuration before starting of fracture, it is needed to apply $\alpha = 0$ and change the L_c to ℓ_c in equation (10).

As dictated by equations (6) to (10), the film configuration and peel force are dependent to the CZ length. Therefore, imposing the boundary conditions of $y(\ell_c) = \delta$ when $\alpha=0$ and $y(L_c)=\Delta$ for the case $\alpha>0$:

$$\begin{cases} \ell_c = \left(\dfrac{24E'I\delta}{T}\right)^{0.25} & \alpha = 0 \\[4mm] L_c = \left(\dfrac{24E'I\Delta}{T}\dfrac{1+\alpha}{1+3\alpha}\right)^{0.25} & \alpha > 0 \end{cases} \tag{11}$$

Therefore, the peel force is determined by substituting the equation (11) into the equation (9).

$$F = \begin{cases} \left(\dfrac{3E'I\delta}{2}T^3\right)^{0.25} & \alpha = 0 \\[4mm] \left(\dfrac{3E'I\Delta}{2}\dfrac{T^3}{(1+3\alpha)(1+\alpha^3)}\right)^{0.25} & \alpha > 0 \end{cases} \tag{12}$$

The onset of steady state (i.e., $\alpha=0$ in equation (12)) is corresponding to the maximum values of peel force, which is dependent to the CZ characteristics and bending rigidity of the film as indicated by equation (13). After starting the steady state, the overall stiffness of the film-adhesive system reduces because of sudden reduction of interface compliance. Sequentially, the peel force shows a reduction and tends to the steady state peel force.

$$F_{peak} = \left(\frac{3E'I\Delta}{2}T^3\right)^{0.25} = \left(\frac{3E'I}{2}GT^2\right)^{0.25} \tag{13}$$

The eccentricity of the peel force with respect to the endpoint of CZ generates an extra moment on film. This moment contributes on the peeling of the film from the substrate and leads the reduction of peel force. The load eccentricity stabilizes at steady state and peel force will be constant. It means the CZ length reaches out to L_S at steady state. Therefore, the maximum value of CZ length ($L_{c,peak}$) is corresponding to F_{peak} and is obtained at $\alpha=0$ as expressed by equation (14).

$$L_{c,peak} = \left(\frac{24E'I\Delta}{T}\right)^{0.25} = \left(24E'I\frac{G}{T^2}\right)^{0.25} \tag{14}$$

The peel angle is set to 90 degree in this and the peel tests presented in by Rezaee et al (2019) [30] provides instructions to achieve this peel angle. The magnitude of load eccentricity factor and CZ length for the steady state is defined as α_S and L_S, respectively. Moreover, the peel force F is eccentric by a ratio of $(1 + \alpha_S)$. Equation (15) expresses the CZ length for the steady state which was derived from the classical Kendall model stating that $F_{staedy} = G$ [68].

$$L_S = \left(\frac{24E'IG}{T^2} \frac{1 + \alpha_s}{1 + 3\alpha_s} \right)^{0.25} \tag{15}$$

To obtain the configuration of the film for the steady state, the equation (4) turns to the following equation [68]:

$$(\alpha_s L_S)^2 = \frac{2E'I}{F}(1 - \sin\theta_L) \tag{16}$$

The term $\sin\theta_L$ in equation (16) refers to the rotation angle of the end point of the CZ as shown in Figure 2-3-b that is calculated as $\tan^{-1}(y'(L_C))$ from the equation (10).

$$\theta_L = \tan^{-1}\big(y'(L_s)\big) = \tan^{-1}\left(\frac{TL_s^3}{12E'I}\left(\frac{1 + 4\alpha_s}{1 + \alpha_s}\right) \right) \tag{17}$$

The deflection of the film in the steady state (h) is expressed by the equation (18) [68]:

$$h = y(L_C) + \frac{\left[\frac{1}{\sqrt{2}}\ln\left[\frac{\sqrt{2} + \sqrt{2 - \lambda^2(1 - \sin\theta_L)}}{\lambda\left(\sqrt{2} + \sqrt{(1 + \sin\theta_L)}\right)} \right] + \sqrt{(1 + \sin\theta_L)} - \sqrt{2 - \lambda^2(1 - \sin\theta_L)} \right]}{\lambda\sqrt{(1 + \sin\theta_L)}} \tag{18}$$

where the $\lambda = x / \alpha_s L_s$.

The deflection of film (h) in the equation (18) is highly dependent to the interface strength (T), bending rigidity of the film, cohesive zone length, and the magnitude of α_s. Since the CZ length and peel force are functions of α, the value of α_s corresponding the steady state can be

obtained by importing the L_S from equation (15) into equation (16) and imposing $F=G$ for the steady state can be stated as equation (19):

$$\alpha_s^2 \left(\frac{24E'IG}{T^2} \frac{1+\alpha_s}{1+3\alpha_s} \right)^{0.50} = \frac{2E'I}{G} \left(1 - \frac{TL_s^3}{12E'I} \left(\frac{1+4\alpha_s}{1+\alpha_s} \right) \right) \tag{19}$$

Given the CZ characteristics and the film's mechanical properties, the magnitude of α_s is identified using a MATLAB optimization solver to find the root of nonlinear equation shown by equation (19).

2.1.3 Results

To examine the model result, for a 3M Scotch tape with E'=1333 MPa, $I=$ $(1\times0.0000508^3/12)$ =1.0925$\times10^{-17}$ m^4, and an adhesive layer with T=0.25 MPa and G=57.4 N/m, the film configuration is shown up to the steady state in Figure 2-4(a). The result of linear and nonlinear bending theories is distinguished by black and red curves in Figure 2-4(a), respectively. The peel angle tends to the 90 degree for peel force extremity.
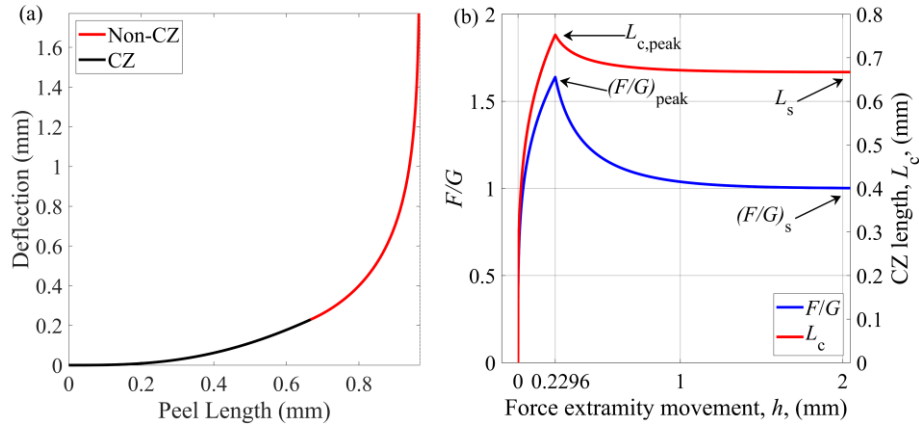
Figure 2-4: Analytical result of peel model; (a) the configuration of the film on the onset of steady state peeling; (b) Representation of normalized peel force and CZ length variations

As discussed earlier in the previous section, the maximum of peel force and CZ length appears at the onset of fracture of the adhesive layer corresponding the separation displacement of $\Delta = G / T = 0.2296$ mm and $\alpha = 0$ as shown in Figure 2-4(b). Plots of CZ length and normalized peel force confirms the stabilization of these parameters at the steady state such that the peak value of the peel force $(F/G)_{peak} = 1.639$ happens at $h=0.2296$ mm (or $\alpha=0$). The corresponding value of peel force eccentricity factor equals to $\alpha_s = 0.4523$ at which the peel force reaches out to the interface toughness (G). Correspondingly, the CZ length changes from its peak value of $L_{c,peak} = 0.7527$ mm to the steady value of $L_s=0.6669$ mm.

As shown in Figure 2-5(a), the film rigidity dominates the film configuration such that softer film are anticipated to experience higher curvature than stiffer films. And, the linear bending theory is more accepted for the films with higher rigidity. The bending rigidity of the film is a significant factor on the peak values of peel force and CZ length although, it is not an effective factor on the steady state characteristics as shown in Figure 2-5(b).
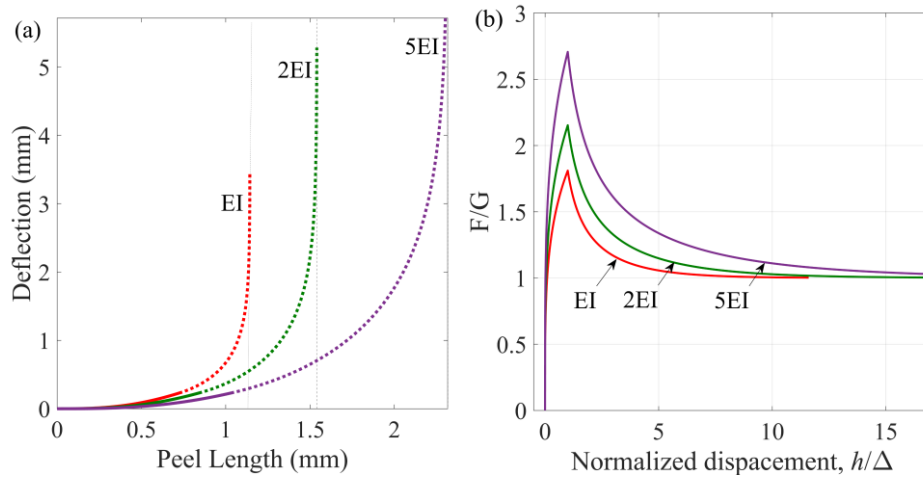
Figure 2-5: effect of the bending rigidity of the thin film on the (a) film configuration and (b) peak value of the peel force

19

The interface toughness of the adhesive layer is a unique characteristic that is only varied by peel rate in the peel test. Therefore, at a given interface toughness and peel force, it possible to identify the corresponding CZ length from the analytical model presented in this study. Then, for each individual G, there are many sets of (F_c, L_c) as shown in Figure 2-6(a) by normalized variation peel force versus normalized length of CZ.

A higher normalized peel force is corresponding to a lower normalized cohesive length. Moreover, for each pair of $\{(F/G_0)_{peak}, L_{c,peak}/L_s\}$, there is a corresponding pair of $\{G, T\}$. Therefore, for each data point of Figure 2-6-a, there is an associated normalized interface traction (T/T0) and a given magnitude of G_0.

Figure 2-6(b) represents the plots based on variable normalized interface toughness (G/G_0) and normalized interface strength (T/T_0) for cases where the normalized peel force are set on specific values. This plot is helpful when the peel force and interface toughness are given but the adhesive layer properties is not specified. Moreover, these plots are helpful to predict the peak value of peel force when the adhesive layer mechanical properties are handy.

Figure 2-6(b) is restructured in Figure 2-6(c) so that each contour is associated with a normalized value of G/G_0, which is helpful to estimate the CZ length and fracture toughness or relate both to a given value of normalized interface toughness.

For instance, for $G/G_0=1$ and $(F/G_0)_{peak}=2$, it is expected to have normalized fracture strength of $T/T_0=1.8$ (following Figure 2-6(b)) and $L_{c,peak}/L_s =1.22$ (following Figure 2-6(c)).
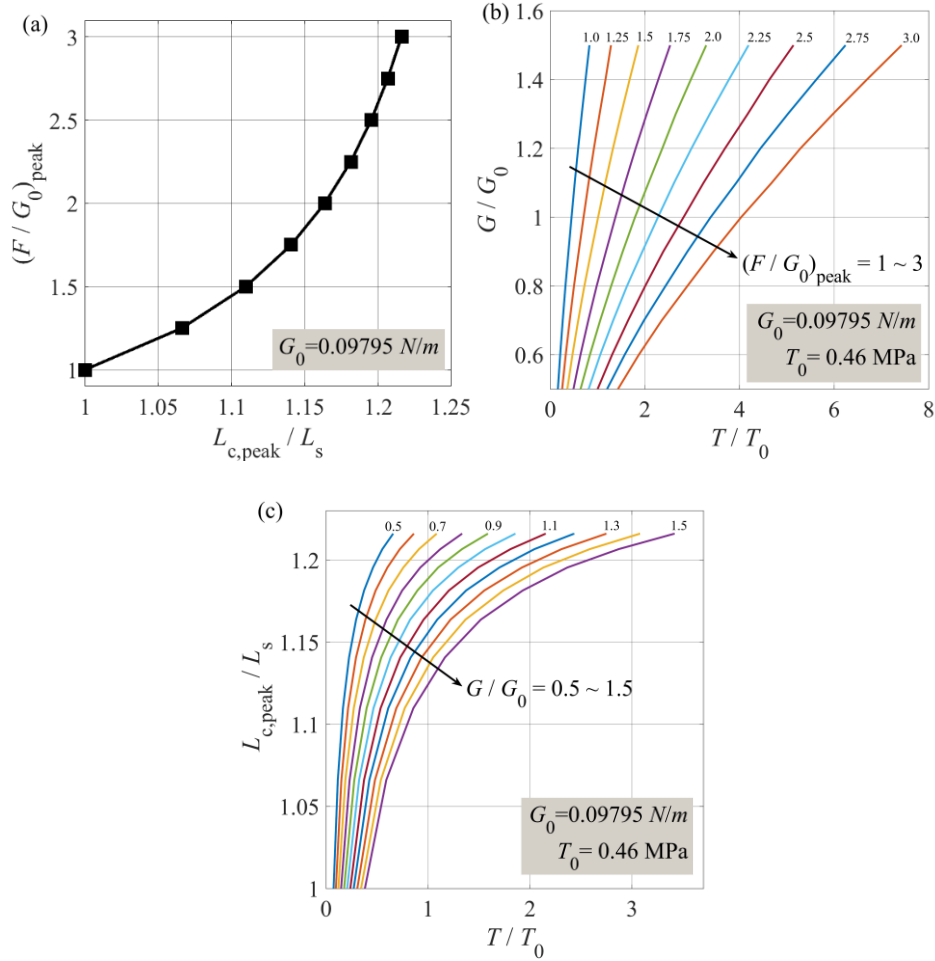
Figure 2-6: The CZ characteristics are highly dependent to the peak value of the peel force through the viscoelastic properties of the adhesive layer; (a) Variation of normalized peak force versus normalized CZ length illustrates independency with respect to variation of interface toughness; (b) Contour plots of normalized peel force based on normalized interface traction and toughness; (c) Contour plots of normalized interface toughness based on normalized interface traction and CZ length

2.1.4 Experimental validation of Semi-nonlinear bending theory

The viscoelasticity of the adhesive layer indicates that the film configuration and interfacial forces are dependent to the peel rate [61,66,74]. To study the peel test mechanics, the main set of peel tests are set on a constant peel rate of 0.1 mm/sec and peel angle of 90 degrees

21

that guarantees a constant interface toughness experiments [30]. Therefore, the values of $(F/G)_{peak}$ and G are easily obtainable from experiments and is pulled into the analytical model to determine the CZ properties.

The results presented in Figure 2-4 are for the peel test of Scotch tape on the bare silicon wafer with the peel rate 0.1 mm/sec. As shown in Figure 2-7-a, the magnitude of $(F/G)_{peak}$ from the test is 1.415 which is corresponding to a fracture strength of T=0.187 MPa. The CZ length for the steady state was calculated as L_c=0.7929 mm and the maximum CZ length was determined by $L_{c,peak}$=0.8703 mm.

Conducting the peel test with same tape and substrate but a peel rate of 5 mm/sec, the $(F/G)_{peak}$=0.1359 was for the interface toughness of G=130 N/m (Figure 2-7-b). The fracture strength was obtained through the model by T=0.586 MPa which is an anticipated higher traction in comparison to the previous peel rate. On the other hand, the CZ lengths were decreased to L_c=0.5545 mm and $L_{c,peak}$=0.6031 mm implying the existence of a shorter CZ for a higher peel rate.

The last sample with the peel rate of 1 mm/sec was analyzed. Corresponding to a $(F/G)_{peak}$=0.1359 and G=130 N/m, the fracture strength of T=0.460 MPa was determined so that the steady state and maximum CZ lengths were obtained by L_c=0.5720 mm and $L_{c,peak}$=0.6342 mm (Figure 2-7-c). Demonstrating the viscoelasticity properties of the adhesive layer, the given results (T, Lc, and $L_{c,peak}$) for peel rate of 1 mm/sec was consistently laid between values obtained for peel rates of 0.1 and 5 mm/sec.
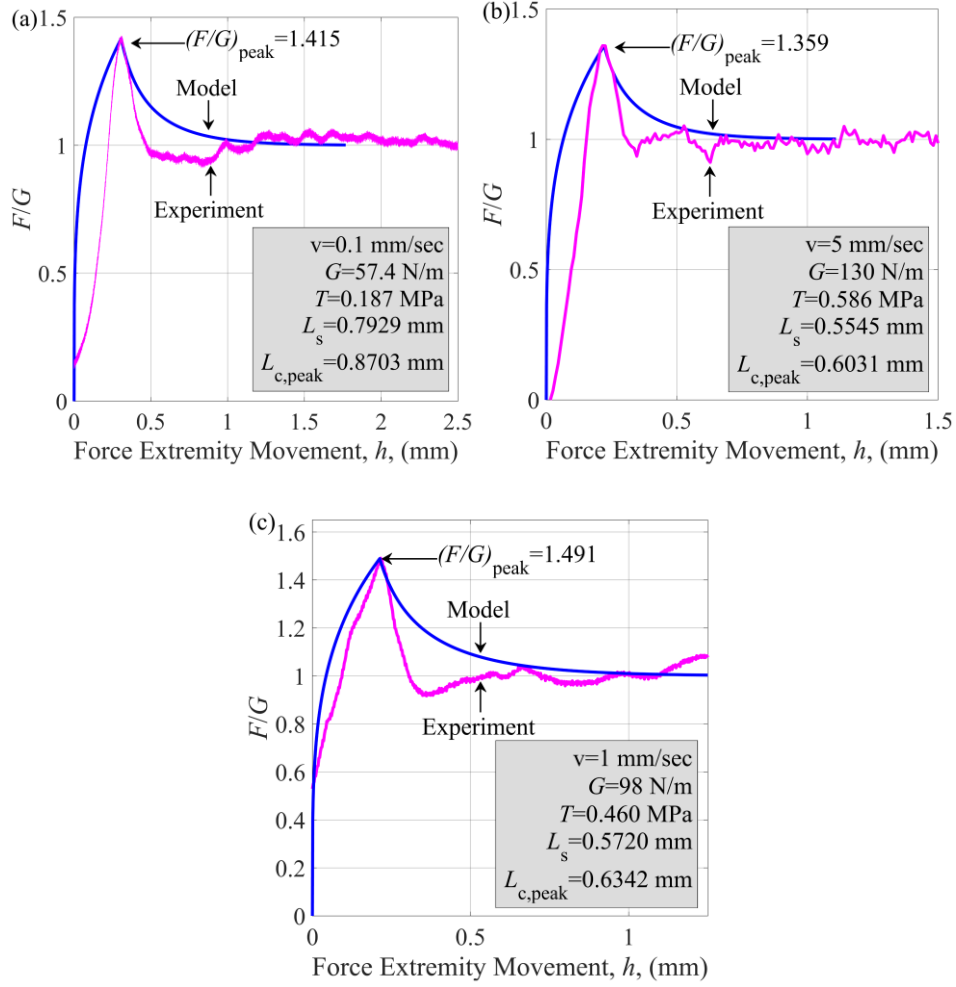
Figure 2-7: comparison of analytical model and experimental result for peeling of Scotch tape form a bare silicon wafer

for the peel rate of (a) 0.1 mm/sec, (b) 5 mm/sec, and (c) 1 mm/sec

As validated by many analytical and experimental studies, the interface variation has shown a logarithmic trend versus the variation of the peel rate as shown in Figure 2-8(a) [30,59,63]. The viscoelasticity of the adhesive layer is the only factor of the peel test setup that affects the interface toughness. As anticipated, for higher peel rate, the CZ lengths reduces confirming the time dependency of the adhesive layer interaction, which could be considerable in very small peel rates. The Figure 2-8(b) illustrates that the maximum

displacement of adhesive layer is an intrinsic parameter such that has not shown significant variation for variable peel rates.
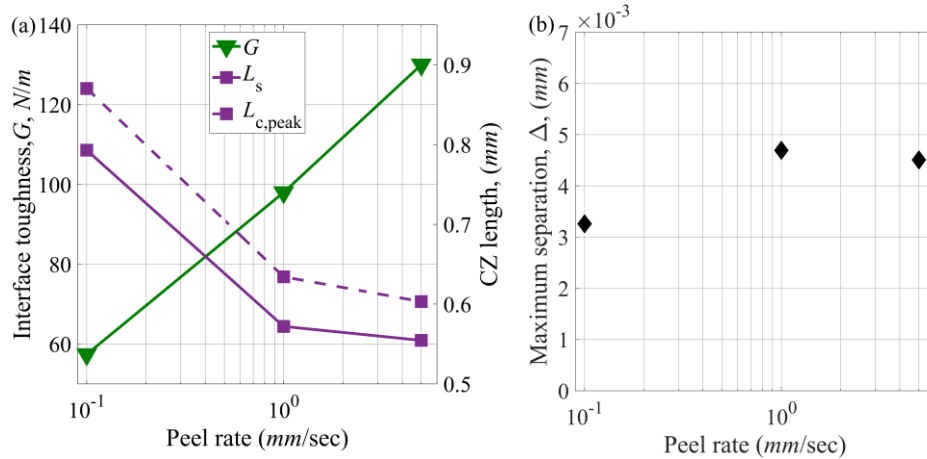
Figure 2-8: Pee rate effects on (a) the adhesive layer properties and (b) maximum separation displacement from peel rate

2.2 Controlled peel test (Methodology and results)

1.

This section presents a controlled peel test and study performed to identify the effects of variation of a range of parameters on the adhesion of tape to a surface. Experimental results illustrate that these parameters can affect the measured bonding forces significantly.

- Peel rate

- Peel angle

- Application pressure and its duration

- The wait time between pressure removal and test start

The objective of this work was to identify controls to minimize variation due to testing techniques.

2.2.1 Methodology

To reach out a repeatable quantitative measurement of the peel force, the experimentation and analysis are employed to determine the significance of the above mentioned factors on the test results. Then, the suggested instructions for the peel test are provided to control key parameters and maximize the consistency.

Based on peel mechanics, literature on peel test, and geometrical analysis provided later in this section, the peel rate and peel angle seem to be most significant factors on the peel force. The peel rate is defined as the velocity of the peel front (or crack propagation along with the cohesive zone). The velocity of the tape extremity is considered as the pull rate. Pull angle (α) is the angle between the force pulling the tape and the substrate (90° in Figure 2-9). Peel angle (θ) is defined as the angle between the tape free from the substrate and the bare substrate surface as shown in Figure 2-9. At a constant peel rate, the individual effects of peel angle is noticeable such that from peel angle of zero to 90 degree, a big variation of peel force was measured [65,66,97–100] while beyond the 90 degree of peel angle, a minor variation of peel force is expected. A power function is reported by many analytical and experimental studies for variation of peel force versus peel angle [65,66,100,101].

As explained above, controlling the peel rate and angle, reduces variation and increases the consistency of the measurements. Therefore the experimental setup is aimed to control peel rate and angle through employing automation and kinematics. To assess all factors effects on the peel force measurements, a full factorial analysis was done based on design of experiment (DOE) to identify other significant parameters on the peel force.

The consistent pull rate was gained by an automated mechanical testing machine (Instron 3369). Basic geometries (Figure 2-9) were found to have non-constant, non-linear relations between pull rate (v) and both peel front velocity ($\dot{x}$) and peel angle (θ) as shown in Figure 2-10(a) and Figure 2-10(b). The tensile test system was equipped with an Omega LCL-010 full bridge load cell to measure the small scale loads. Then, independent of ambient conditions, the peel force is quantified for the peeling of tape from a substrate.
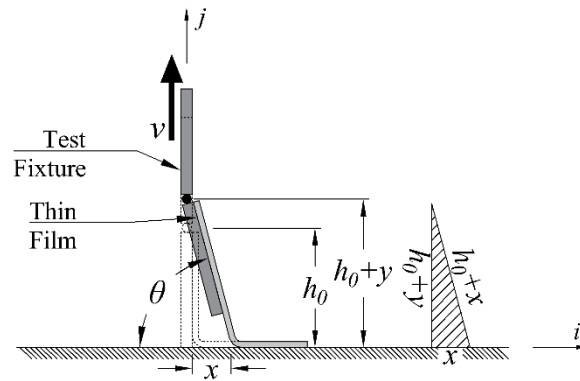
Figure 2-9: Schematic view of straight pull tests that starts with initial peel arm of h_0 and peel angle of 90°. The peel rate ($\dot{x}$) and peel angle (θ) change nonlinearly during test that the hatched triangle demonstrates the relationship between pull rate (v), peel rate ($\dot{x}$), peel angle (θ), and vertical movement of tape extremity (y) [30]

Basic straight pull: non-linear rate and variable angle

Through introducing a local coordinates system, the geometrical properties and relations are expressed based the substrate surface (aligned with <*i*>), the tape extremity surface (aligned with <*j*>). Since the peel angle was set up on 90°, this local coordinate systems presents a Cartesian system. The horizontal <*i*> movement of the peel front by distance of

$x = y + (y^2/2h_0)$ causes the relative peel angle of $\theta = \tan^{-1}((h_0 + y)/x)$ and peel rate of $\dot{x} = v(1 + y/h_0)$ to vary nonlinearly with time as well as reorienting the peel force vector.

the parameters h_0 and y are in Figure 2-9 for the straight peeling geometry. Figure 2-10(a) and (b) clearly show that both the peel rate and the angle change significantly at a constant pull rate in this configuration.
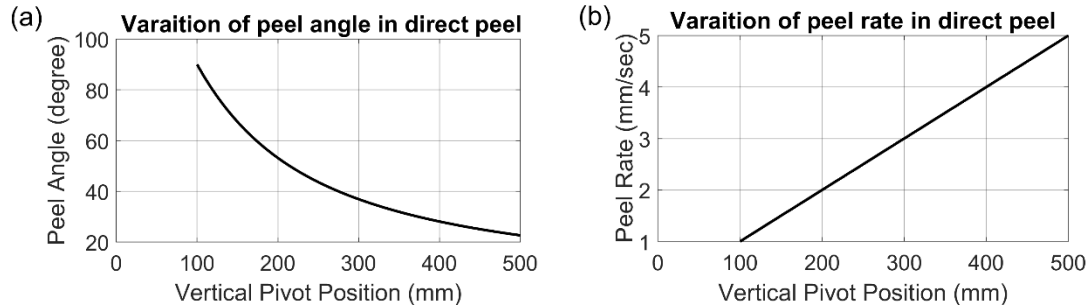
Figure 2-10: Variation of peel angle and peel rate for straight peel test. The variation of (a) peel angle and (b) peel rate for the straight peel geometry. These plots are drawn for a nominal h_0= 100 mm and a constant pull rate $v = 1\ mm/sec$.

[30]

Employing larger h_0 would reduce the nonlinearity such that for $h_0 \to \infty$, x and θ will approach y and 90° respectively, and $\dot{x}$ would approach v. To overcome the nonlinearity of peel rate and angel, it was necessary to have at least h_0=500mm, which introduces major experimental issues for the test. Moreover, the small nonlinearity of peel rate and angle would affect the peel force significantly [66,100,102]. Therefore, having another tests setup was necessary in which the peel rate and angle variations are controlled.

Angle control

Keeping the assumption of inextensible thin film that reasonable for small peel force [32,54,65,69,103,104], it is necessary to relate the peel angle (θ) and peel rate ($\dot{x}$) to the pull angle (α). Considering the peel front movement in Figure 2-11, the relationship of peel front movement and extremity movement can be obtained by $x = y[\cos\alpha / (1 - \cos\theta)]$. Triangle DEF, $x = y(\sin\alpha / \sin\theta)$ provides another relation between x and y. Combining equations for x and treating y as a constant as desired, the desired pull angle can be calculated as $\alpha = (\pi - \theta)/2$ which creates constant peel rate and peel angle. For testing purposes, a jig was constructed that would rotate the frame of reference to align the pull direction vertically, for the tensile tester, and provide a desired slope for the substrate. As shown in Figure 2-12, the jig angle equals to $(\pi/2 - \alpha)$ which is equivalent to $\theta/2$. Based on this, a jig and test setup were constructed for further testing and analysis, with a slope of 45° to maintain a 90° peel angle.

The 90° peel tests studied in this study relates the measured pull force (F_{pull}) per width (W) of peel arm to a corresponding energy release rate of $F_{pull}(1 - \cos\theta)/W$, as originally introduces by Rivlin[105]. Also, it has been reported that the relation between the peel force and the peel rate follows a power law equation at a constant peel angle of 90° [65,66,100,101]. Based upon a discretized model suggested by Xia et al[69], the peel force is significantly affected by peel angle as following:

$$\varepsilon = \sum_{i=1}^{N} \int_{S_{i-1}}^{S_i} \frac{1}{2} D_i \big(\beta'(s)\big)^2 ds - \int_0^{S_N} F_{pull}(\cos(\beta - \theta) - 1)ds - \int_0^l G\, ds \tag{20}$$

Three terms in equation (20) show works done by bending of peel arm, pull force, and adhesion energy respectively, where ε is the potential energy, $D(s)$ is the distribution of bending rigidity, and G is the constant adhesion energy. In addition to peel angle (θ), the curvilinear angle of peel arm (β) is another significant factor on potential energy[104] which is corresponding to the peel front angle at $s = 0$ as represented in Figure 2-11. Above equation indicates the significance of the peel angle on the peel force such that the peel force significantly changes from peel angle of zero to 90 degree[65,66,97–100] and beyond the 90 degree of peel angle, a minor variation of peel force is expected.

2.2.3 Results

To reach out an optimal instruction for the peel tests for small-scale application, a set of experimentation was done to inspect the individual and combinatorial effects of effective factors on the peel force. All results presented here, unless otherwise specified, were produced with 3M Scotch® Magic™ tape 810 (with the width and total thickness of 19 mm and 0.060 mm respectively) on PolyTetraFluoroEthylene (PTFE) and PolyEther Ether Ketone (PEEK) substrates. Since this study is targeted bonding evaluation of rGO layers on the flexible substrate, it is necessary to navigate peel test toward some potential candidates for substrate. The substrates has provide appropriate flexibility and surface bonding properties, a high enough survival temperature, an inert bed for deposition, and low price.
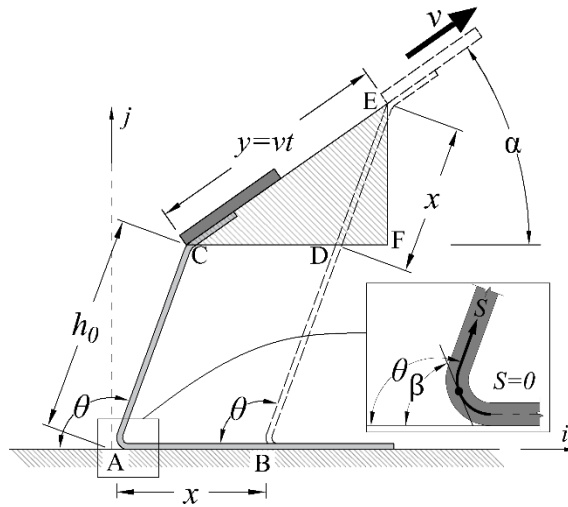
Figure 2-11: Geometric view of controlled peel test in which the constant peel angle of θ (and sequentially the constant peel rate of v) requires the pull force to be applied in angle of α. [30]
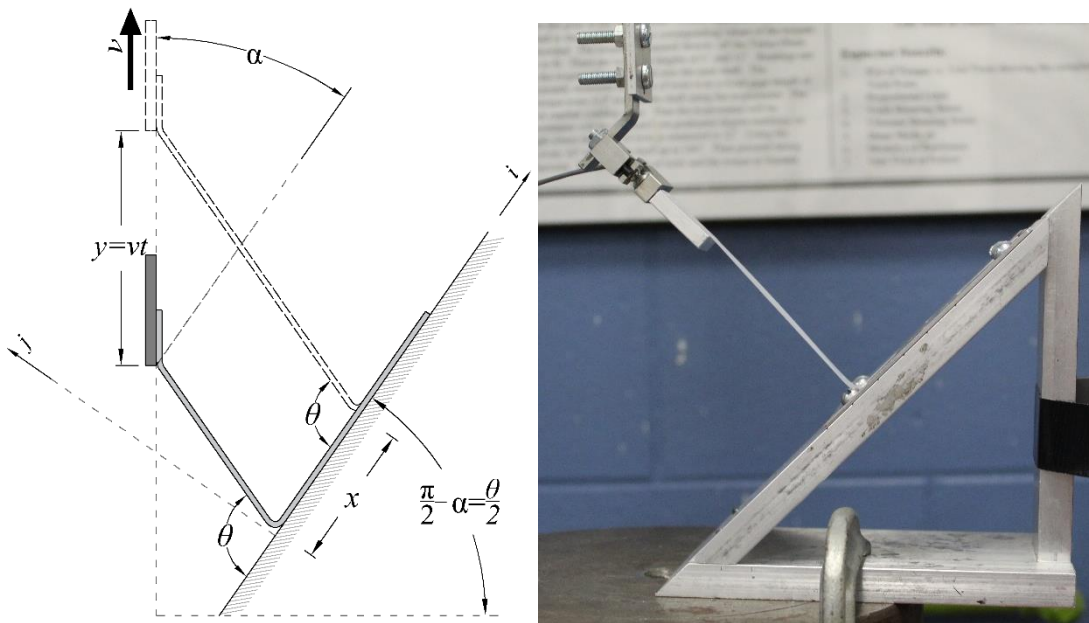
Figure 2-12: The substrate must be rotated by the angle of θ/2 since the pull force is applied just in vertical direction. [30]

based on experimental results and literature, the peel rate is the most significant factor on the peel force [65,75,106,107]. This dependency come from a noticeable variation of CZ length versus peel rate such that a higher peel rate is corresponding to a shorter CZ and higher interface traction, which in result causes higher peel [108].

Multiple tests were performed with controlled, constant peel rates ranging from 0.01 to 10 mm/sec. The range was limited at the low end by the sensitivity of the load cell, and at the high end by the capabilities of the Instron. Inspection of the results presented in Figure 2-13 found that the relation between the average peel force and peel rate followed a logarithmic trend with coefficients of determination (R^2) of 91.2% and 92.0% respectively. The logarithmic variation in Figure 2-13 requires to control the peel rate during the peel test as a significant factor on the peel front failure energy to achieve consistent peel force and repeatable experimentation. The trends of peel force variation versus peel rate have validated the previously reported trend as explained in literature[65,66,100,101].
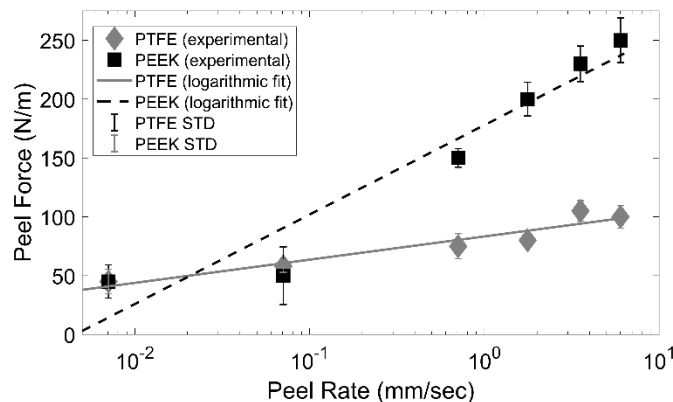
Figure 2-13: A logarithmic trend of peel force variation versus peel rate for both PTFE and PEEK demonstrating that the peel force is a highly rate-dependent parameter. [30]

31

Magnitude of application pressure

Although, a few studies mentioned the application pressure as a significant pressure factor on the peel force[64,75,109], the effects of application pressure on peel force have not been studied individually. The application pressure reduces the small bubbles and heterogeneity of the adhesive layer that makes it a uniform and more consistent layer. The resulted uniformity is expected to help to reduce the variation of the peel force measurement.

A rubber pad is employed to impose uniform pressure on sample within a predefined pressure. Magnitudes of 0, 29, 60, and 81 kPa were applied with the other typical parameters producing the peel force results shown in Figure 2-14(a). The results show that the magnitude of pressure when adhering tape to a substrate can have a large effect on the peel force up to a point, above which the pressure does not alter the peel force. Beyond 30 kPa for the application pressure, the peel force has not shown significant differences. It demonstrates that the 30 kPa of application pressure is an appropriate choice. To being a bit conservative and guarantee the air bubbles removal (and uniformity of adhesion layer), the application pressure is set on 81 kPa for the experimentation.

Duration of application pressure

Tests on the effects of the duration of application pressures on the peel force of tapes for durations of 1, 2, 4, 8, and 12 minutes producing the results shown in Figure 2-14(b). The results show that the variation in peel force is considerable for pressure durations up to 4 minutes, beyond which the peel force showed negligible variation. Based on this result, a minimum pressure application time of 4 minutes was selected to minimize variation.

32
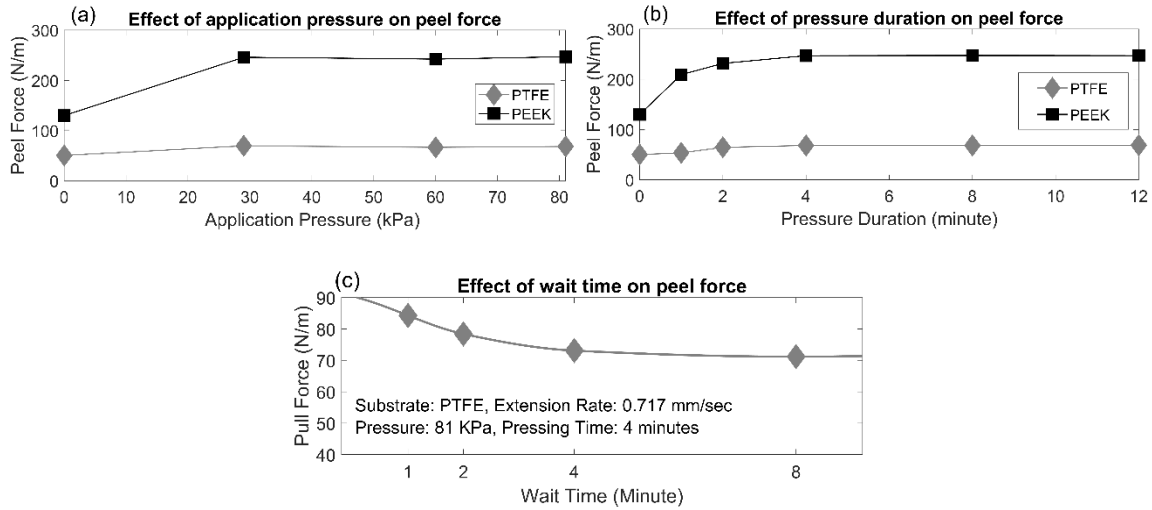
Figure 2-14: Significant factors on peel force; (a) application pressure effect on the peel force for PTFE and PEEK; in these experiments the peel tests are done after application of pressures for 8 minutes including 4 minutes of pressure duration and 4 minutes of wait time, (b) application duration effect on peel force for PTFE and PEEK is evaluated with pressure of 81kPa in addition to 4 minute of wait time, and (c) wait time effect on peel force for PTEF is assessed considering pressure of 81 kPa during 4 minutes. [30]

Waiting time

The wait time between the removal of the application pressure and initiation of peeling test was also varied to determine its effect on peel force. An approximate time of one minute is needed to remove pressure form sample and mount it on the test fixture. Then, a minimum wait time of one minute is expected for each test. Giving more time to adhesive layer is corresponding to more time of recovery for the adhesive layer to return to its initial situation (before application of pressure) but with more uniformity and less air bubbles. As shown in Figure 2-14(c), the wait time also has influences peel force, though it is smaller than the effects of the magnitude of application pressure and duration. Like magnitude and duration of the application pressure, the wait time approached a constant value with slight variation beyond

4 minutes. This suggests that the tape relaxed after removing the application pressure and waiting a minimum of 4 minutes would reduce potential variation in peel strength due to the wait time. A few studies mentioned the wait time in different ranges like a few minutes[101], 20 minutes[65], and a day[75].

Factorial analysis

The experimentation was set up based on a 3^k factorial analysis in which the main effects of each factor and their combinatorial effects on the peel force are analyzed to rank the significant parameters on the peel force. Through employing the suggested design for the peel test, the peel angle is no longer a significant factor on the peel force.

These experiments addressed the magnitude of tape application load, duration of application load, and peel rate at three levels each as is shown in Table 2-1. The experiments used 3M scotch® Magic™ 810 tape on PTFE and PEEK substrates. The effect of wait time was significantly smaller than the other factors, providing a maximum variation of 15 N/m compared to hundreds of N/m for the other factors. Therefore, wait time was kept at a constant 4 minutes and not varied in the factorial analysis.

Parameter	1st Level	2nd Level	3rd Level
Velocity (mm/sec)	0.141	0.707	3.535
Pressure (kPa)	29	60	81
Duration (minutes)	1	2	4

Table 2-1: The three levels factorial analysis parameters

34

The peel rate or velocity was tested at magnitudes of 0.141, 0.707, and 3.535 mm/sec, controlled by the Instron MTS machine. A uniform and distributed application pressure was applied on the tape through a rubber pad with preset magnitudes of 29, 60, and 81 kPa. These pressures were applied for durations of 1, 2, and 4 minutes. Introducing the significant factors on the peel force, the peel rate, magnitude of application pressure, and the duration of application are three effective factors, respectively. These are confirmed by the Pareto charts based on a 3-level factorial analysis of the extreme values shown in Figure 2-15(a) and (b) for both substrates. The reference lines in Figure 2-15 identify the significance level of each factor in factorial analysis such that factors with lower effect than reference line is not statistically significant. Combinatorial interactions of the 3 parameters studied were found to be smaller than any of the individual effects according to the factorial analysis.
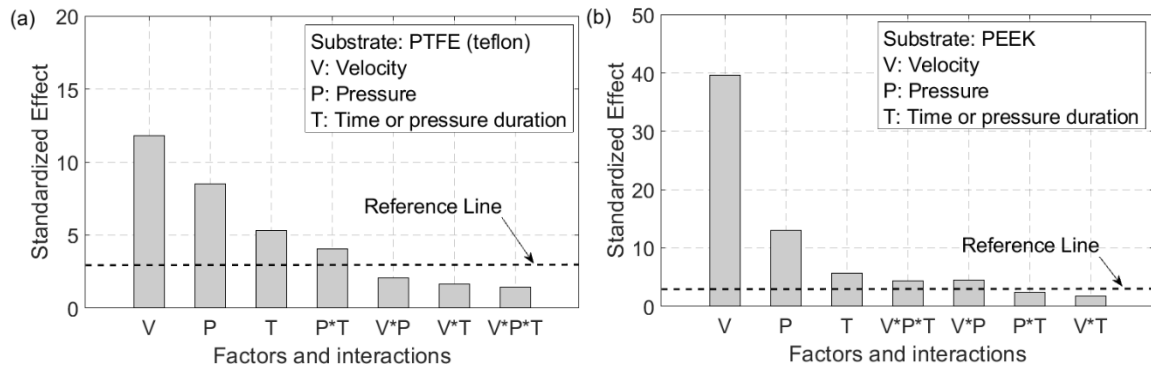
Figure 2-15: Normal effects plots showing all three factors of peel rate, application pressure, and pressure duration have a significant effect on peel force whereas the interactions are not significant that much. (a) plot for PTFE substrate and (b) plot for PEEK substrate. [30]

2.2.4   Consistency and evaluation of proposed setup

As shown in the prior sections, the magnitude of the peel force was affected by the duration of applied pressure, magnitude of applied pressure, and wait time between removing

35

the application pressure and testing. The consistent measurement of peel force requires these factors to take a minimum value beyond which no significant variation of peel force is anticipated. Based on the results of this testing a pressure with a minimum magnitude of 30 kPa should be applied for a minimum duration of 4 minutes, a minimum of 4 minutes should elapse between the pressure removal and peel testing to produce consistent forces. Additionally, peel rate and peel angle have drastic effects on the peel force and therefore must be controlled.

The next experimentation was designed to assess the consistency of the suggested design and instructions for the peel test. The experimentation was conducted considering different peel rate and above-mentioned instruction for application pressure and its timings. Then, the application pressure of 81 kPa was applied on samples for four minutes and samples were rested for another four minutes after pressure removal.

The coefficient of variation (CV) is defined in two ways in this study:

1. *intra-test CV*

   The variation of peel force while it is considered for a single test (and apparently a single substrate). As shown by dotted line in Figure 2-16(a) and (b), it was calculated for the steady state peel force in a single test.

2. *inter-test CV*

   The variation of mean value of peel tests after onset of steady state for several tests with the same factors of peel test. As presented by dotted line in Figure 2-16(c) and (d), it was calculated across the mean forces produced by multiple similar tests.

36

As can be seen in the data in Table 2-2 and Figure 2-16(a)-(d), higher peel rates had a higher consistency and lower CVs for both analyses with both substrates. Closer examination revealed that the standard deviation of the peel forces remained relatively constant across peel rates while the mean peal force increased with peel rates resulting in a reduction in the CV with increased peel rate. Looking at the cohesive zone in micro scale, at lower peel rates, the filaments of adhesive layer behave more actively which leads to dominant asynchronous failures of filaments along the width of the tape.

The average magnitude of inter-test CV for PTFE and PEEK are about 6 and 8 percent respectively, and are smaller at higher peel rates demonstrating improved consistency compared to the reported magnitude variation of 37% by ASTM D-3359[110].

Substrate	CV (%)	Peel Rate (mm/sec)					
		0.007	0.071	0.707	1.768	3.353	6.010
PTFE	intra-test	8.270	6.257	17.530	9.203	11.913	10.480
	inter-test	21.444	10.640	16.966	5.575	8.439	11.125
PEEK	intra-test	10.423	12.737	15.963	10.453	6.610	7.743
	inter-test	32.843	30.745	4.492	7.028	4.966	6.304

Table 2-2: inter-test and intra-test CVs for PTFE and PEEK
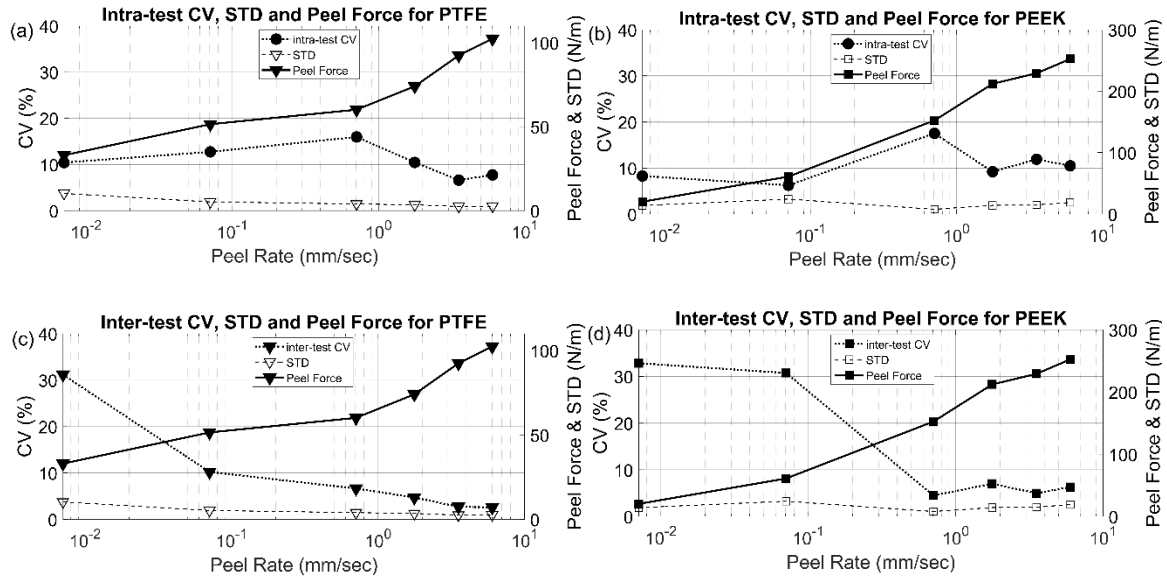
Figure 2-16: Coefficient of variations are calculated through experiments demonstrating an acceptable consistency of result given form proposed setup for peel test. (a) & (b): the intra-test CV trends changed to a decreasing trend after peel rate of 0.707 mm/sec for both PTFE and PEEK demonstrating that the asynchronous failures of filaments of adhesive layer is much lower in for peel rate around 1 mm/sec and beyond; (c) & (d): an inverse trend of inter-test CV in comparison to peel force is obtained for both PTFE and PEEK demonstrating higher consistency of proposed test method at higher peel rates; For all plots the standard deviation is roughly similar showing that the significant factors on peel force are well-controlled. [30]

2.2.5   Testing peeling of a thin latex paint layer

In this section, the results of peel test are shown for a plastic thin film deposited on the PTFE substrate. The Behr latex paint was applied to PTFE to create a thin film that would peel off of the substrate with an adhesive failure. Four hours after deposition, peel tests were conducted based on suggested instruction on samples with dimensions of 19×25.4 mm (¾ by 1 inch). The peel rate of 0.141 mm/sec was set up. Figure 2-17 represents four phases of peel front failure. The direct peeling of tape from the bare substrate is defined as the first phase. In the second phase the tape was peeling from the film and the film was also peeling

38

from the substrate forming a little bubble under the film as shown in Figure 2-17. The contribution of bending rigidity of both tape and paint layer and membrane action of un-detached region around the peel front lead to highest peel force for the second phase in comparison to other phases. Phase 3 began when the film detached from the substrate at one end and began a complete peel from the substrate at a single point. Phase 3 had a lower peel force than phase 2 but higher than phase 1. This phase acts a transient phase to complete peeling of paint layer from the substrate. In phase 4 the plastic film was peeling from the substrate without tape backing it. A big drop of measured force occurred at the start of phase 4 due to the low axial stiffness of the film resulting in a substantial increase in strain, i.e., the film elongated with minimal peeling. This effect disappeared quickly, and the peel rate returned to the initial value regenerating the peel force, which was consistent for the remainder of phase 4. The difference of phases highlights the sensitivity of the method developed, even detecting the force required to bend the tape. The lack of variation in phase 4 compared to the other phases was attributed to the change in peel mechanism. In phase 1 the tape was peeling directly off of the substrate and a roughly randomized failure of filaments of the adhesive layer at the peel front region caused variations in the peel force[62,103,104,111]. Phases 2 and 3 also had effects of bending a multi-layered beam with viscously bonded layers. Phase 4 consisted exclusively of the dry film bending and peeling off of the substrate without the soft and variable adhesive layer which created a relatively constant force.
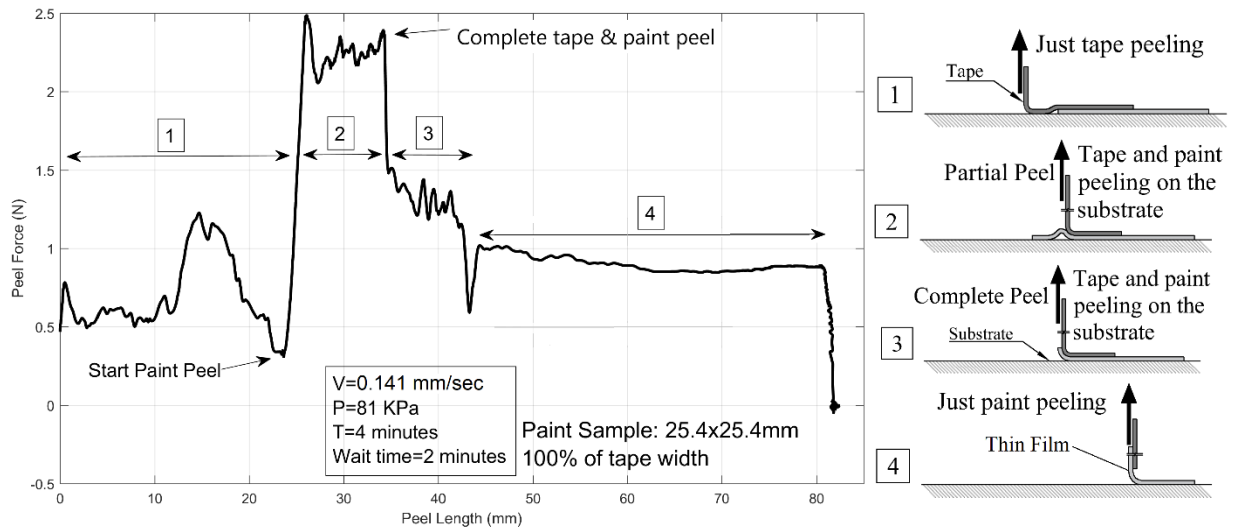
Figure 2-17: A layer of 1 by 1 in. of Latex paint on PTFE substrate is tested and for phases of peeling were observed; 1) peeling of tape from substrate, 2) partial peeling of tape and paint from substrate which is included with extra bending and elongation of paint layer. These led to variable local peel angle that makes this case sophisticated, 3) peeling of tape and paint from substrate and 4) peeling of paint layer from substrate which is much more consistent that other modes because of lack of adhesive layer. [30]

2.3 Failure modes characterization

The peel test is being done by measuring the fracture energy released at the peel front. The released energy contains of multiple possible failure modes at the interface of the tape and deposited layers (or the substrate). These modes can be categorized in two general adhesive and cohesive failures that are discussed elaborately later this chapter.

2.3.1 Failure modes

In this study, considering the visible remnant rGO particle on the tape back, a methodology is developed to distinguish between failure modes. The cohesive failure are addressed by visible particles on the tape back in which the interlayer fracture occurs between

rGO layers. Considering this definition for the cohesive failure, the following failure modes could be included in the cohesive failure:

- rGO/rGO interlayer failure

- rGO/substrate interlayer failure

On the other hand, in the rest of sample where there are no visible peeled particles, the adhesive failure is considered. Based on this definition, the big variation of adhesive energy is expected since the following modes might be included:

- tape/substrate interface failure

- tape/rGO interface failure

- rGO/rGO interlayer failure (but invisible)

2.3.2 Sample preparation

Considering a high flexibility, appropriate elastic modulus, excellent thermal survivability, and acceptable electro-chemical properties, Kapton (polyimide) was selected for the experimentation. Sheets of Kapton HN500 (DUPONT, thickness of 127 μm) were cut to dimensions of 3 cm x 1.5 cm (4.5 cm^2) and the surface of each piece was rinsed with distilled water. The Kapton substrates were then treated with O_2 plasma using a Plasma Etch PE-25[112] at 50 Watts for 5 min to activate the surface for bonding which also made it more hydrophilic (Si-OH). The O_2 plasma-treated Kapton substrates were immediately immersed in a 2% solution of 3-aminopropyltriethoxysilane (APTES)[113] (A3648, Sigma-Aldrich, St. Louis, MO, USA) prepared in ethanol for specific amounts of time as noted in the

41

experiments, resulting in an amino-functionalized substrate (Si−OH−NH$_2$) which would bond with the functional groups (COOH) of carbon nanomaterials.

A commercially available GO solution (Graphenea, Graphene Oxide Water Dispersion 0.4 wt.% concentration) was diluted with ultrapure water (UPW)[112–115] (Milli-Q System, Millipore, USA) to 2 mg/ml. The UPW has a specification of 18.18 million ohm-cm at 25℃. The GO solution was placed in a Cole Parmer M-Series sonication bath [116]for a specific amount of time to ensure dispersion and then drop cast onto the prepared Kapton substrates. The GO-Kapton samples were then dried in an oven at 36℃ overnight. Finally, the GO-Kapton samples were reduced in an argon environment with temperature ramped to 350℃ in 10 minutes and then held for 5 minutes.

2.3.3   Image processing

Since the amount of rGO particles left on the tape back plays important role on failure modes definitions, the analysis of amount of peeled rGO particles along the sample is done using an image processing technique.

Photographing

The first step after conducting the peel test is taking images of the rGO particles left on the tape back (Figure 2-18(a)). To have a clear image, the tapes are transferred to a transparent sheet and then on a light pad before taking image. Photographing is done using a Canon EOS digital camera from vertical distance 300 mm. Finally, the images are converted to 8-bit (or Grayscale) images to be prepared for next steps as shown.
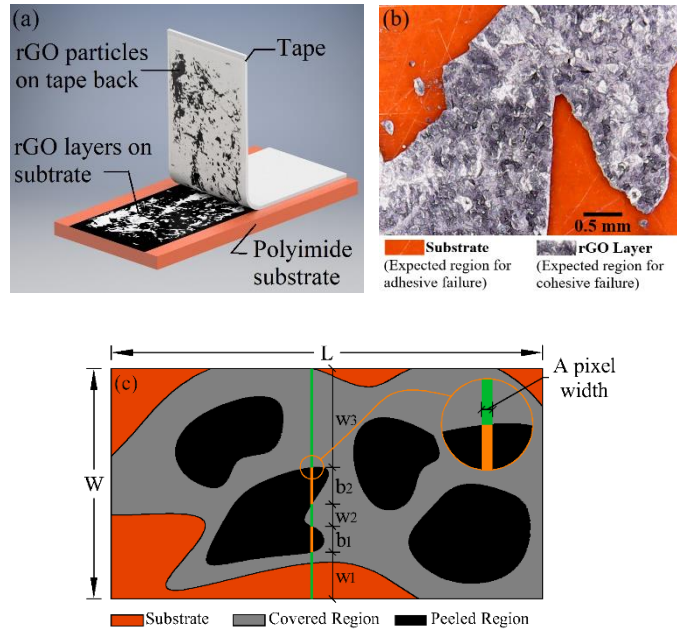
Figure 2-18: rGO peeled from substrates with multiple failure modes; (a) schematic view of peeled rGO particles stuck on back of tape during peeling; (b) photograph of a sample with mixed mode failure; (c) schematic of tape back showing the regions indexed with w_i is corresponding to the contribution of the equivalent adhesive failure and the regions indexed by b_i refers the equivalent cohesive failure [117].

Threshold-base image processing

Since the peel force variation is expected to be corresponding to the amount peeled rGO, and the peeled rGO particles are observable on the tape back, an image processing technique is utilized to quantify the remnant rGO particles on the tape back.

As shown in the photograph in Figure 2-18(b), there was a visible distinction between regions of bare substrate vs. regions where rGO remained on the substrate, indicating adhesive failure at the rGO –substrate interface vs. cohesive failure of the rGO itself, respectively. Assuming a strip with the width of a pixel and overall length of W as shown in Figure 2-18(c), the normalized ratios $\sum b_i /W$ and $\sum w_i /W$ can be determined for each strip and identified as percentages of cohesion and adhesion contribution for each measurement, respectively.

The ratio of $\sum b_i / W$ is anticipated to vary from zero to one in which the zero refers to pure adhesive failure and one is associated with pre cohesive failure. As the images are converted to 8-bit images, the color indices along the sample changes from zero for pixels with black color to 255 for pixels with white color. The Figure 2-18(a) shows that the base color of image background is not completely white. Considering the base color index coming from the tape material, which is about 75, it considered as the threshold of the image processing. Therefore, the pixels having indices lower than 75 are considered as rGO particles and the rest of pixels do not contain rGO particles.

The image processing code will implement an algorithm to detect the pixels containing indices lower than threshold as rGO particles. The border shown in Figure 2-18(a) illustrates the edges of the sample and confines the analysis in its inner region. The following are results from the image processing code:

- The overall percentage of rGO particles peeled off from the sample is calculated by counting ratio of number of pixels containing rGO over the overall pixel number of the sample. For instance, for the sample shown in Figure 2-19, the 32.87% of whole sample area is associated with cohesive failure. This percentage will be defined as overall cohesive failure later.

- The profile of amount of peeled rGO particles is the most important result of the image processing code. It represents the variation of rGO (or cohesive) failures along the sample. Sequentially, the profile of unpeeled regions (or adhesive fracture zone) can be identified easily just by subtracting the peeled rGO profile from the overall width of the sample as shown in Figure 2-19(b).

44

- What is the coverage percentage rGO particles for each sample? This percentage will be defined as effective covered area later.

- The actual percentage of peeled rGO with respect to the effective covered area. This value will be defined as effective peeled region.
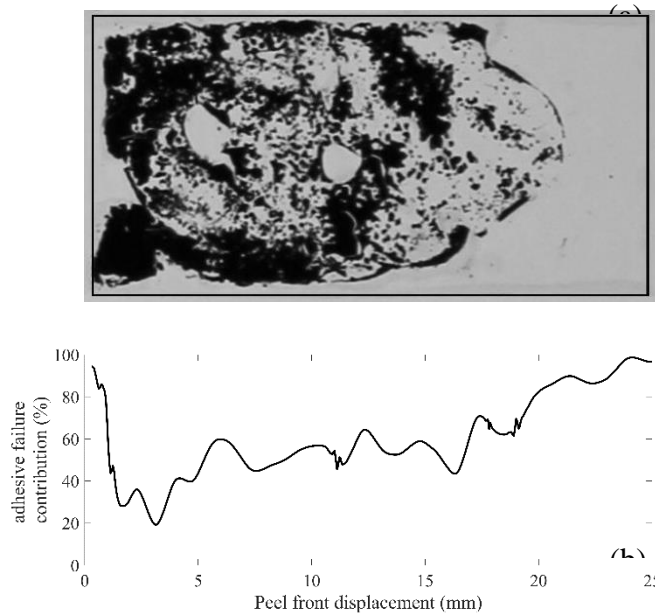
Figure 2-19: image processing result representation; (a) 8-bit image of sample and (b) the profile of adhesive failure contribution on the peel front energy release (k1411b22-190920) [117]

2.3.4 Correlation of the peel force and adhesive failure

Although, interlayer bonding forces (i.e. cohesive energy) of rGO layers initiates from weak bonding forces called Van der Wall forces [118], the adhesive forces are from the adhesive layer that follows the CZ characteristics. Therefore, the adhesive failure is expected to have more contribution on the peel force such that the variation of peel force might be correlated to the variation of the contribution of the adhesive failure mode on the peel front failure. This

correlation was examined through the comparison of pattern of the adhesive failure profile and the pattern on the peel force variation as illustrated in Figure 2-20 and the correlation of 80% was identified between the profiles of the adhesive failure and peel force.
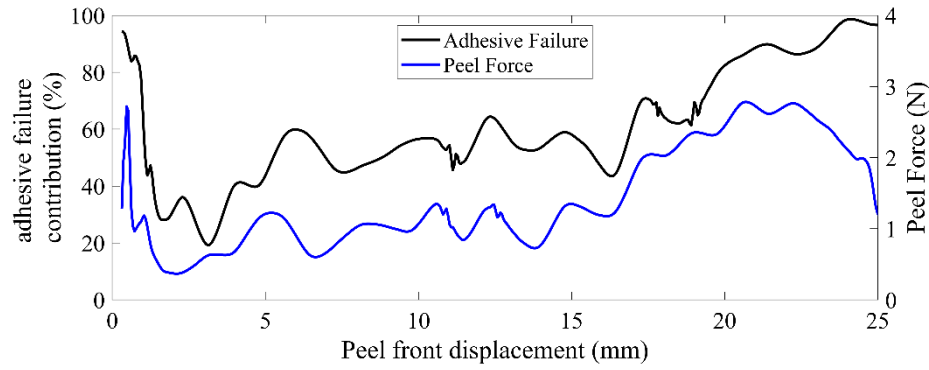
Figure 2-20: correlation between peel force profile and adhesive failure profile [117]

The correlation value changes with the variation of the overall cohesive failure ratio so that for the samples with a high ratio of peel rGO, the correlation value goes high up to 98% which looks helpful fact for failure mode characterization.

2.3.5 Mathematical model

In the classic Kendall's model[54,68], the peel force is equivalent to the bonding force for the peel angle of 90 degree. Considering the Dugdale cohesive zone (a constant T-S model) [70,84], the mathematical model presented in equation (22) expresses the measured force based on two general modes of adhesive and cohesive failure. The index j represents the jth measured force while the index i shows image processing result at the jth measurement.

The peel force measurement at each time pixel is called f_j. From the image processing results, $\sum w_i$ and $\sum b_i$ represent the number of pixels associated with adhesive and cohesive failure, respectively. Considering the model assumptions, the amount of adhesive failure

energy is considered non-constant along the sample and is called G_j, which is strongly dependent the $\sum w_i$. The cohesive energy, g, is assumed constant along the sample that is only dependent to interlayer energy of rGO particle and apparently thermal reduction factors.

$$f_j = G_j w_j + g b_j \quad (j = 1,2,\dots,n)$$ (22)

Generally, the following failure modes are expected to contribute on the overall peel energy (G):

- the adhesive failure between tape and substrate (G_{T-S})

- the adhesive failure between tape and rGO layers (G_{T-G})

- the cohesive failure of invisible rGO layers which is embedded in total adhesive failure (G_{G-G})

On the other hand, the g may contain G_{G-S}, G_{G-G}, and G_G as discussed in literature. Expansion of Equation (22) to a matrix form in Equation (23), illustrates that there are n equations for each f_j with $n+1$ unknowns in the model (including G_j and g). Therefore, another equation is needed.

$$\begin{bmatrix} w_1 & 0 & \cdots & 0 & b_1 \\ 0 & w_2 & & \vdots & b_2 \\ \vdots & & 0 & \vdots & \\ 0 & \cdots & 0 & w_n & b_n \end{bmatrix} \times \begin{Bmatrix} G_1 \\ G_2 \\ \vdots \\ G_n \\ g \end{Bmatrix} = \begin{Bmatrix} f_1 \\ f_2 \\ \vdots \\ f_n \end{Bmatrix}$$ (23)

The mean peel force, defined as shown in equation (24), was used to provide the necessary additional equation for systems of equations (23). In equation (24) w_m, b_m, and f_m are mean values of adhesive and cohesive widths and peel force respectively that are simply obtained from image processing and peel force measurements.

$$w_m G_m + b_m g = f_m \tag{24}$$

$$\frac{w_m}{n}(G_1 + G_2 + \cdots + G_n) + b_m g = f_m \tag{25}$$

The assumption of mean state of peel force was examined thought existing peel tests result and confirmed by an accuracy of 99%. Equation (24) was rewritten as equation (25) and inserted into equation (22) to complete the mathematical model for calculation of bonding energies as shown in equation (26).

$$\begin{bmatrix} w_1 & 0 & \cdots & 0 & b_1 \\ 0 & w_2 & & \vdots & b_2 \\ \vdots & & 0 & \vdots & \\ 0 & \cdots & 0 & w_n & b_n \\ \frac{w_m}{n} & \frac{w_m}{n} & \cdots & \frac{w_m}{n} & b_m \end{bmatrix} \times \begin{Bmatrix} G_1 \\ G_2 \\ \vdots \\ G_n \\ g \end{Bmatrix} = \begin{Bmatrix} f_1 \\ f_2 \\ \vdots \\ f_n \\ f_m \end{Bmatrix} \tag{26}$$

Equation (26) computes the cohesive failure energy and the profile of variation of adhesive failure energy along the sample based on peel forces and image processing results.
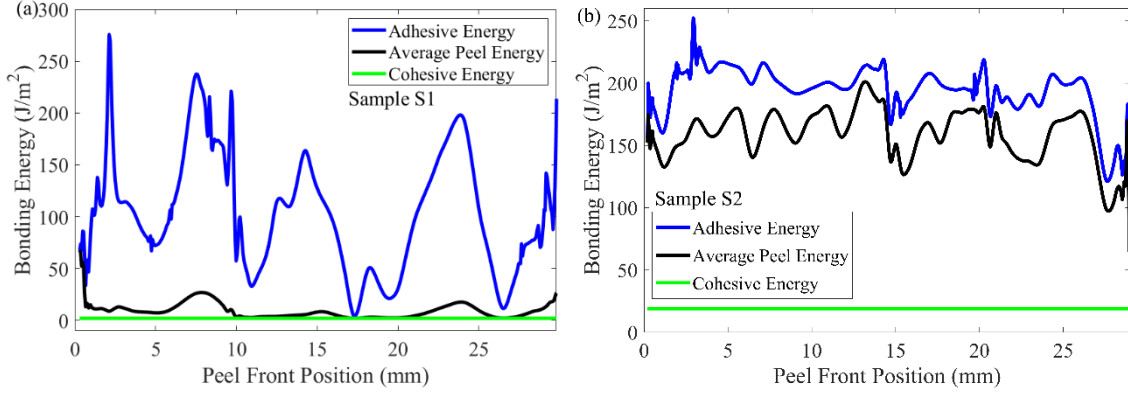
Figure 2-21: Calculated bonding energies for (a) sample S1 and (b) sample S2 including adhesive failure energy (G_j) that was drawn by solid lines, cohesive failure energy (g), and average failure energy ($f_i / (w_i + b_i)$) [117].

The peel force is dominated by the contribution of failure modes at peel front. Higher amounts of remnant rGO particles, corresponding to a high overall cohesive failure (OCF) ratio, enforces the average peel energy toward cohesive energy and lower values of OCF

pushes the average peel energy to adhesive energy. The average magnitude of peel force is defined based normalizing peel force over the width of sample. Based on image processing result, the width of sample may non-constant along the sample and it determines by $(w_j + b_j)$. Therefore, the $F_j / (w_j + b_j)$ represents the average peel force. As shown in Figure 2-21(a), the adhesive energy is much higher than the cohesive energy, dominating the total peel energy and it is reasonable to expect high correlation between the average peel force and the adhesive energy variation in high values of OCF. This correlation will be increased for samples with lower OCF ratios (like Figure 2-21(b)).

The result of the model for sample S1 is shown in Figure 2-21(a). The cohesive failure energy is calculated as 1.951 J/m^2 as well as the average adhesive failure energy of 105.497 J/m^2. The noticeable fluctuation of adhesive energy illustrates significant contribution of all defined failure modes in the adhesive layer for a sample with low cohesive layer. For the sample S2, since the contribution of adhesive failure on peel force is significantly higher than cohesive failure, more uniform values were observed for adhesive failure energy and average peel energy. A dominantly higher cohesive failure of 19.001 J/m^2 was determined for sample S2 with average failure energy of 194.341 J/m^2 as shown in Figure 2-21(b). Moreover, the OCF ratio shows its significance on the bonding energy such that a lower OCF is expected for higher cohesive bonding.

Chapter 3: Bonding Evaluation of Graphene-Oxide Layers

As elaborated in previous chapters, three major steps have been done: 1) demonstration of optimum instruction for the peel test, 2) analytical model of peeling based on nonlinear bending theory, and 3) a mathematical model development to connect the as bridge between experiment and analytical mode. The main goal of this chapter is extending the geometric analysis of rGO particles left on the tape back through an image processing technique. It helps to identify the bonding characteristics of the rGO layers for variable thermal processing parameters. The methodology will be applied on frequent samples to determine what parameters are significantly affecting the mechanical strength of electronic devices made by thermally reduced graphene oxide.

3.1 Experimentation

The rGO samples for this work are made using thermal processing of GO solution in the Argon environment. There are some factors for the thermal processing method that affects the final product. These factors are listed below and tabulated in Table 3-1 :

1. Substrate type: for this study, several substrates were tested initially to produce final candidates. Then, the experimentation is done for final candidates. The following substrates were tested as potential candidates initially:

    a. Silicon

    b. Kapton (Polyimide)

    c. Teflon (PTFE)

    d. PET

e. PEEK

f. PDMS

For the experimentation, the silicon, Kapton, and Teflon were selected based on following consideration:

a. Surface bonding energy

b. Flexibility

c. Availability

d. Cost

2. Surface treatment: employing O_2 plasma and APTES treatment in different duration, the surface treatment is done.

3. GO concentration: the concentration of GO plays key role during thermal processing such that the final product will be affected significantly by this factor as discussed later in this chapter.

4. Sonication time: to prepare the nanofluid GO solution, the sonication has been utilized. The duration of sonication is a critical factor in the thermal processing such that the samples with high sonication time (more than 30 minutes) were observed with low mechanical stability as discussed later.

Table 3-1: thermal processing factors

Factor	substrate	Oxygen plasma	APTES time (minute)	Sonication time (minute)	Temperature (°C)	GO concentration (μg/cm^2)
Levels	Silicon	No	No	60	400	178
	Kapton	Yes	overnight	90	350	222
	PTFE		180	120	280	333
	PEEK		110	180	210	444
			100			
			80			

The objective of this chapter is to develop a methodology to connect mechanical performance of rGO samples to the thermal processing factors. At the end of chapter, the significant factors on the mechanical performance of rGO samples will be introduced.

3.2 Geometric analysis of rGO samples

The configuration of rGO particles left on the tape back contains information about the mechanical stability of thermal processing parameters. The geometric analysis is based on analysis of amount and arrangement of rGO particles left on the tape back. Obviously, this analysis is for visible rGO particles. To visualize the rGO particles on the tape back, the following steps are done:

1. Sticking the with remnant rGO particles to the transparent sheet.

2. Placing the transparent sheet on the light pad.

3. Photographing of transparent sheet on the light pad using a digital camera by a vertical distance of 300 mm.

4. The photos will be cropped and edited to be ready for the image processing.

3.2.1 Parametric bonding analysis

After cropping of photos and converting then to 8-bit photos, an image processing technique is employed to determine the following information for each sample:

- The overall area of sample (A_1 in Figure 3-1).

- The area of sample that is covered by rGO particles before the test (A_2 in Figure 3-1).

- The overall percentage rGO particles left on the tape back in comparison to overall area of the sample (A_3 in Figure 3-1).

- The profile of amount of peeled rGO along with the sample length.

The above information from the image processing is essential for the parametric analysis of rGO samples as elaborated in next sections.

Substrate (A_1)
Graphene (A_2)
Peeled Region (A_3)
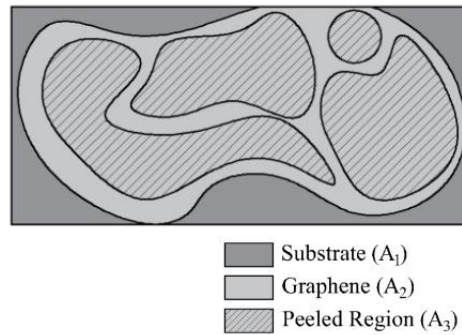
Figure 3-1: schematic view of results of the image processing

Overall Cohesive Failure (OCF)

The ratio of total amount of the rGO particles peeled from the sample over the whole sample's area is defined as Overall Cohesive Failure (OCF). This ratio is identified as A_3/A_1 based on Figure 3-1 and illustrates the percentage of cohesive failure over the whole sample area and can be informative about the mechanical stability of rGO/substrate bonding characteristics.

Effective Covered Area (ECA)

The effective covered area is defined as the ratio of the area covered by rGO layers over the whole sample area, which is determined by A_2/A_1 based on Figure 3-1. It is the important

factor for demonstration of the significance of the thermal processing parameters on the area of regions covered by the rGO layers.

Effective peeled Region (EPR)

The ratio EPR identifies how much of the rGO particles was peeled from substrate. The difference of OCF and PER is that the EPR is measured over the region covered by the rGO layers whereas the OCF is calculated over the whole sample area by A_3/A_2 based on Figure 3-1. The EPR ratio concentrates on the mechanical survivability of rGO layers considering the various thermal processing parameters.

Performance ratio (PR)

Although the above factors represent information about mechanical performance of rGO samples, there are combinatorial effects of ECA and EPR ratios that makes hard the interpretation of result. Moreover, these factors are affected dominantly versus variation of thermal reduction factors. Therefore, the performance ratio (PR) is defined to unify all factors in an individual factor. The PR is determined as ECA/EPR= A_2^2 /A_1A_3.

Variation PR ration is shown in Figure 3-2 versus OCF and EPR ratios. The performance ratio has shown a regulated variation versus OCF and EPR ratios in Figure 3-3. It illustrates that the performance ratio of rGO samples significantly varies by the amounts of cohesive failure and percentage of peeled particles such that lower ratios of OCF and EPR are corresponding to higher performance ratios. On the other hand, the performance ratio has not shown any regulation with variation of ECA ratio as shown in Figure 3-3.
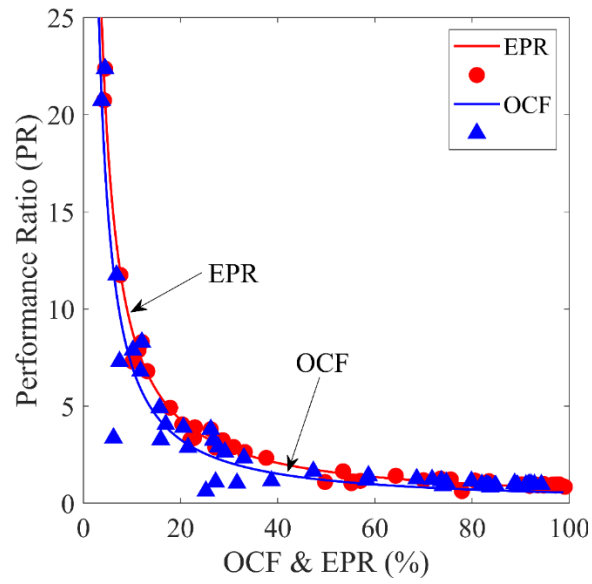
Figure 3-2: variation of PR versus OCF and EPR ratios
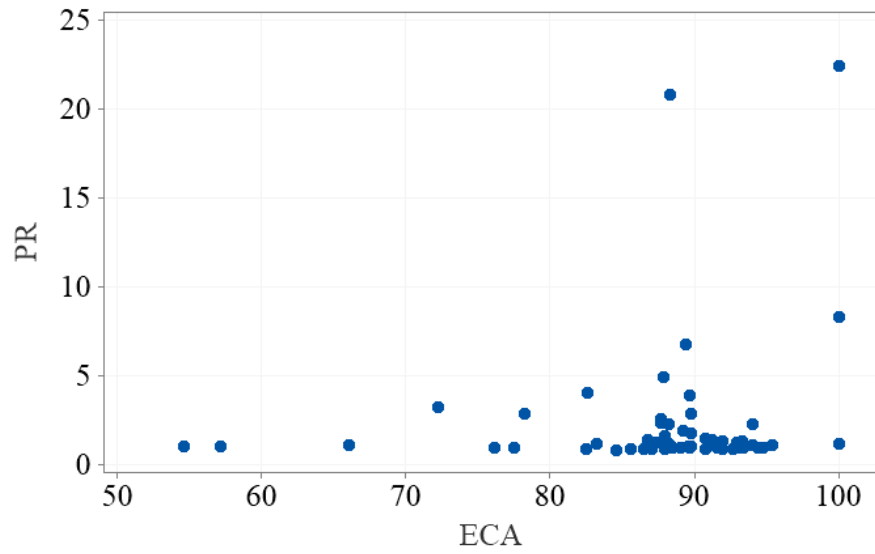
Figure 3-3: variation of PR versus ECA ratio

3.3 **Employing the mathematical model to distinguish between cohesive and adhesive failures modes**

In section 2.3, the mathematical model was elaborated, which was developed to connect the experiments to the image processing results. This model utilized the correlation of peel force variation with the amount of peeled rGO particles. The magnitudes of adhesive and cohesive failure energies, as the results of mathematical model, are determined for samples with different geometric properties of failure (such as OCF, ECA, EPR, and PR ratios) and different thermal processing factors. Conducting the mathematical analyses, will lead to identify the significant factors and properties of rGO samples on the mechanical strength of samples.

3.3.1 Bonding variation with geometric properties of failure modes

As main goal of developing mathematical model, the connection between boding energies and geometrical properties of failure modes is discussed in this section. The geometric factors of OCF, EPR, and PR were defined to provide a tool for analysis of amount of rGO particles peeled off of substrate, which is referred to the cohesive bonding. Therefore, from the mathematical model, the corresponding values of bonding energies are obtained for each set of geometric factors. The cohesive bonding energy has shown meaningful variation versus OCF and EPR ratios such that for lower percentages of both OCF and EPR ratios, higher cohesion energies is anticipated. As shown in Figure 3-4, the variation is good fit with power function trend (with a validity of R^2=0.99) that illustrates small increasing of OCF and EPR ratios are equivalent to significant reduction cohesion energy. For instance, for OCF ratio of 5%, the cohesion energy of 200 J/m^2 is expected while for 40% of OCF ratio, the cohesion energy is reduced to 30 J/m^2. On other words, 35% increase of OCF ratio was equivalent to

56

85% reduction cohesion bonding. The above values of cohesion bonding were determined for rGO samples on the Kapton (polyimide) substrate with processing temperature of 350 ℃ and O_2 plasma treatment for the substrate's surface.
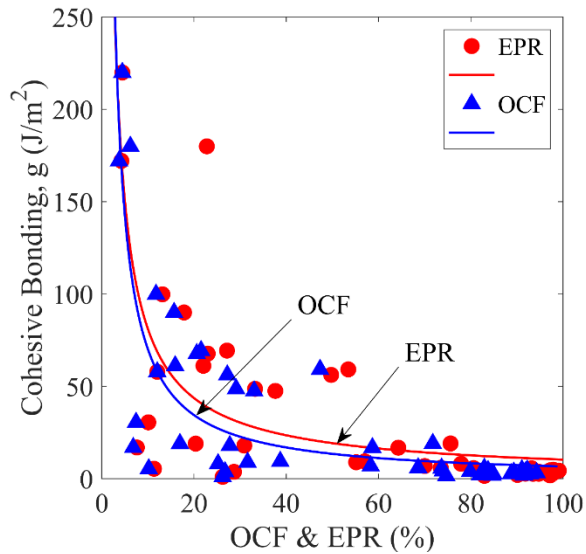
Figure 3-4: cohesive bonding variation with OCF and EPR ratios

Considering the definition of adhesive bonding that includes multiple adhesive-related failure modes, it is anticipated to have big variation of adhesive energy along with the sample. Figure 3-5 shows the variation of adhesive energy (by blue curve) along a sample with high OCF ratio (about 90%).
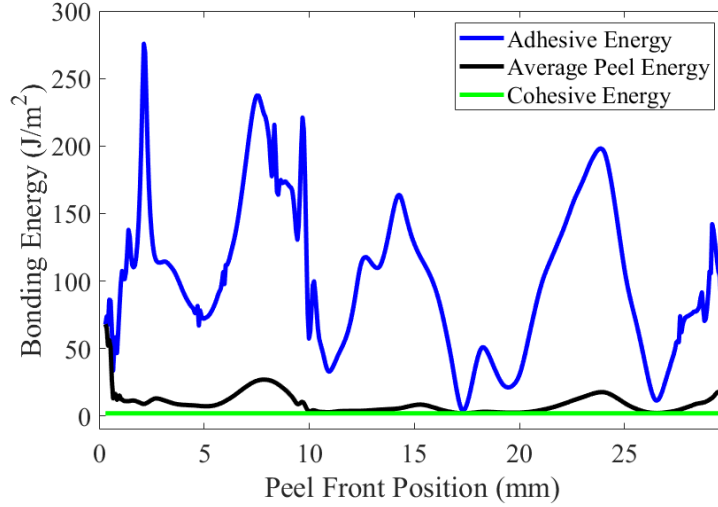
Figure 3-5: big variation of adhesive bonding energy along with the sample

Moreover, extracting an average value for adhesive bonding energy per rGO sample, expands the variability of measurement. As shown in Figure 3-6, with a high variability, higher adhesive bonding energies are expected for small ratios of OCF (or EPR) factor.
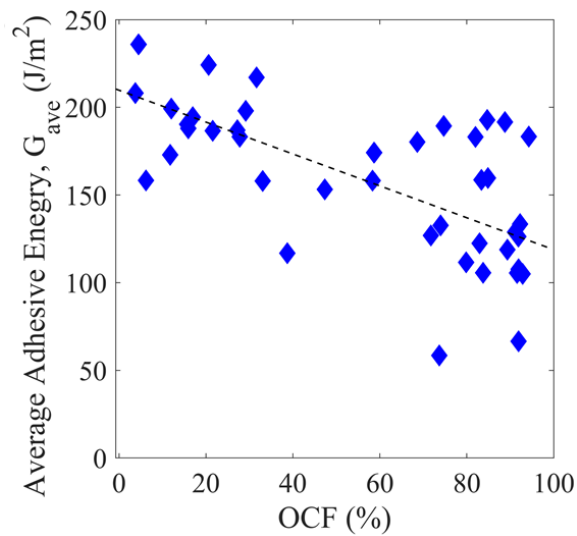
Figure 3-6: adhesive bonding variation with OCF and EPR ratios

Figure 3-7 shows the overall assessment of bonding energies based on overall cohesive failure (OCF) ratio for rGO samples deposited on Kapton (Polyimide) substrate with processing temperature of 350 ℃ under O_2 plasma surface treatment. The cohesive failure has shown high dependence to the OCF ratio with a power function regression model and validity of 99% as shown in Figure 3-7(a). Interestingly, both major bonding energies, i.e., cohesive, and average adhesive energy, has illustrated good interaction with together such that a higher cohesive energy is corresponding to a lower average adhesive energy. This regulation was validated by a power function regression model with 94% in Figure 3-7(b). Considering the high range of variation for adhesive bonding energies, as elaborated above, having a meaningful relation between two major bonding energies demonstrates the effectiveness of developed mathematical model.
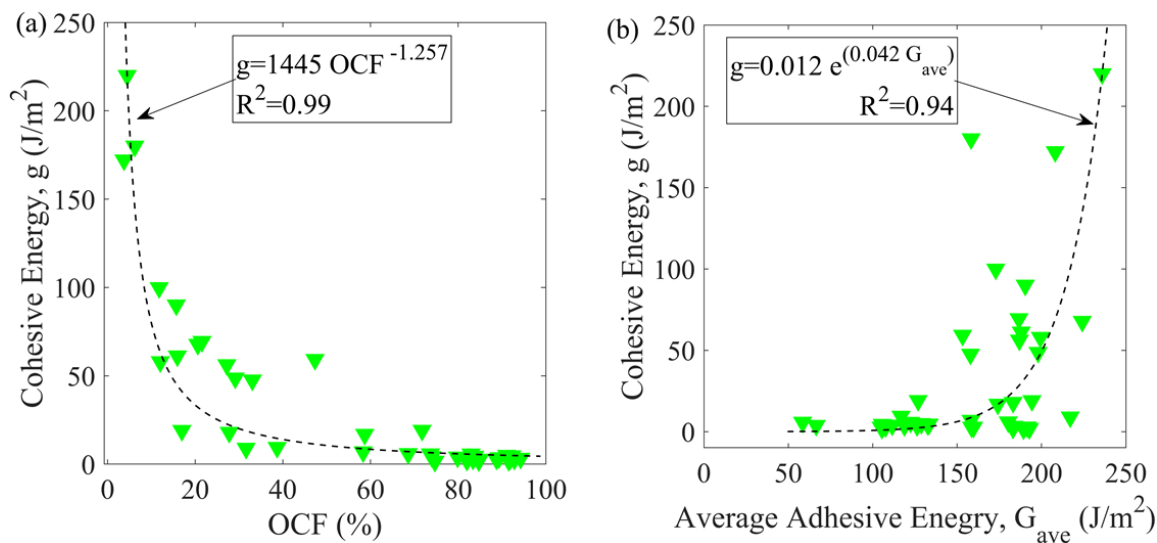
Figure 3-7: bonding energy assessment for rGO samples on Kapton (polyimide)

The PR ratio showed a roughly linear dependence to cohesive failure energy which looks a reasonable outcome form mathematical model (Figure 3-8). It demonstrates that the

performance ratio can be considered as a good index to assess the cohesion energy of rGO layers qualitatively. Adding results for other substrates into account demonstrates that the above-mentioned variation model of PR versus OCF (in Figure 3-7(a)) is validates for other substrates such as Silicon, Teflon, PEEK, and PDMS184 as shown in Figure 3-9. The same is expected for the variation of PR ratio versus EPR ratio.
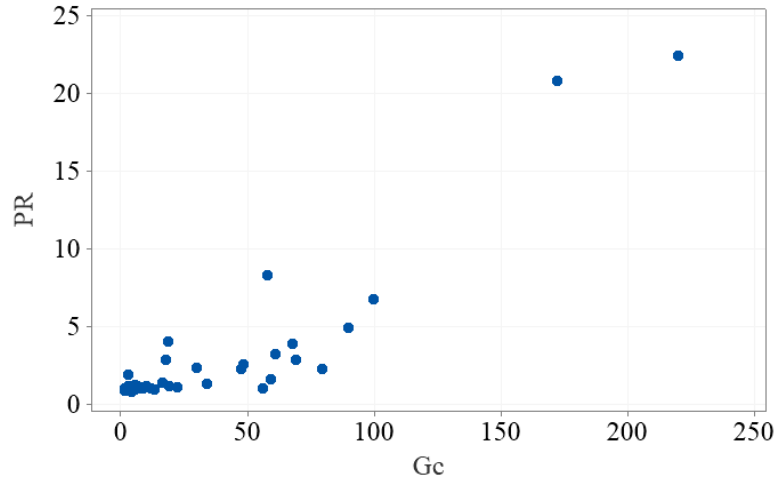
Figure 3-8: variation performance ratio (PR) with cohesive bonding energy
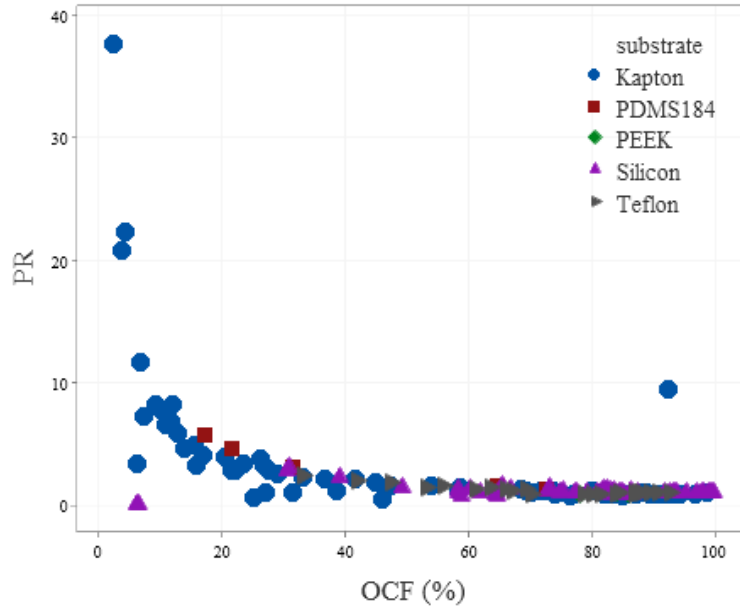
Figure 3-9: variation of PR ratio versus OCF ratio for multiple substrates

The PR ratio did not show any regulation with the average adhesive failure energy which refers to its high variation along the sample (Figure 3-10).
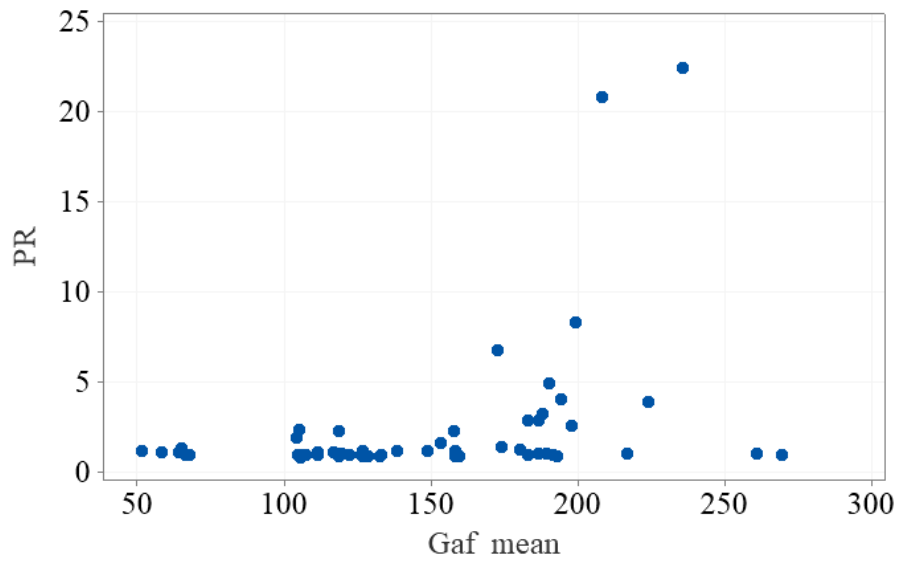
Figure 3-10: variation performance ratio (PR) with average adhesive bonding energy

3.3.2 Effects of thermal processing factors on PR ratio

In this section the results of ANOVA analysis are presented to identify the effects of thermal processing factors on the performance ratio of rGO samples.

Looking thoroughly over the magnitudes of PR ratio in Figure 3-11 for Kapton, Teflon, and silicon substrates illustrates the noticeably higher performance ratio of Kapton in comparison to other substrates. Moreover, the optimal value of GO concentration is different per substrate. Kapton has shown the highest PR ratio of about 8 at the lowest GO concentration (i.e., 178 $\mu g/cm^2$). This is a reasonable result so that higher values of GO concentration leads to increasing the GO layers and reduction the mechanical stability of sample. Therefore, it is anticipated to have better performance of samples for lower concentration GO. It is confirmed for Silicon and Teflon substrates such that the best performance was given for GO concentration of 222 $\mu g/cm^2$ as illustrated in Figure 3-11.
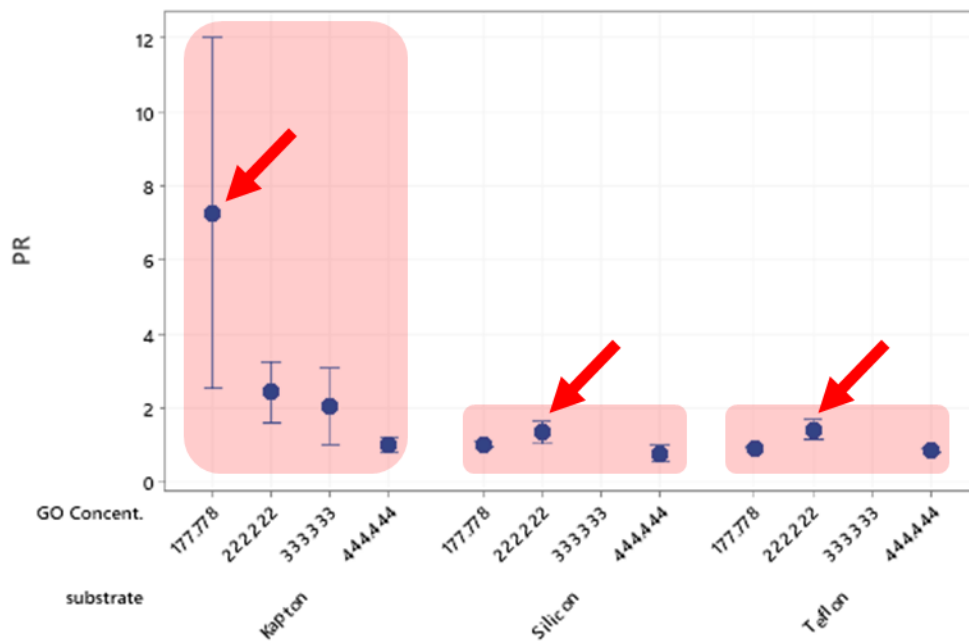
Figure 3-11: variation performance ratio versus GO concentration for three substrates

62

Another factor is the sonication time, which has not shown significance on the PR ratio but, it is significant factor on the OCF ratio as shown Figure 3-12. The plot shows that the lowest sonication time led to lowest OCF ratio. The literature and new set of experiments demonstrated that the sonication time of less than 30 minutes is the best range for the sonication duration.
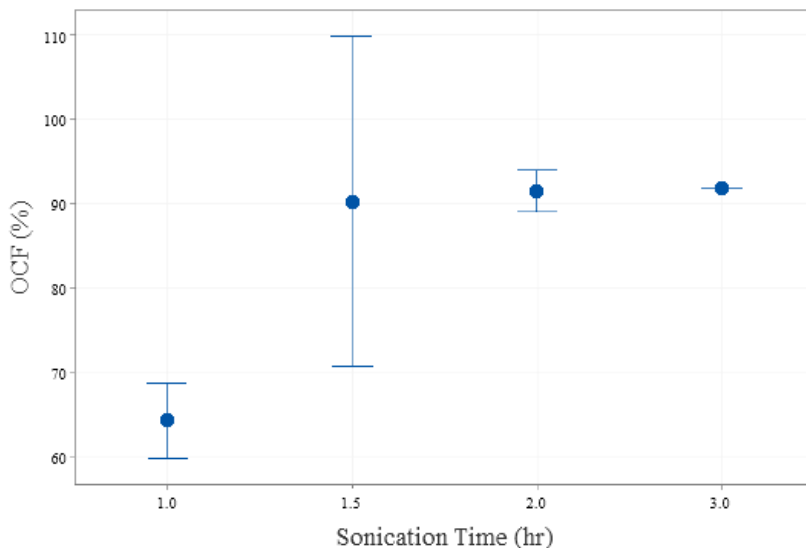
Figure 3-12: significance of sonication time on the OCF ratio

The PR ratio varies significantly versus duration of APTES treatment. The analytical study illustrates that the optimal duration of APTES treatment would in a range of 100~110 minutes considering results for all substrates as shown in Figure 3-13.
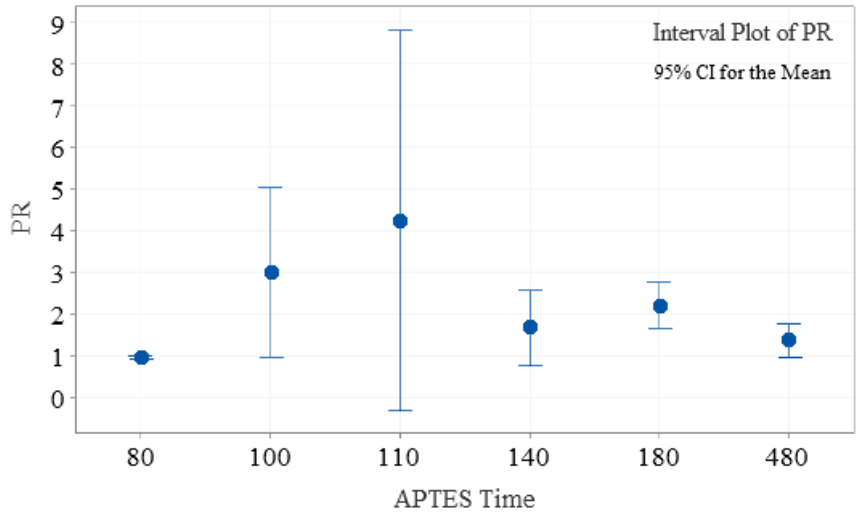
Figure 3-13: variation PR ratio versus duration of APTES treatment

To gather the comparative study results, the significant factors on the mechanical stability of rGO samples are identified based on result of geometric analysis. The results are provided for four substrates of Kapton, Teflon, Silicon, and PDMS. The curly brackets in Figure 3-14 are the optimal range of thermal processing factors base on the geometric analysis:

Substrate	APTES treatment duration (min)						GO Concent. (µg/cm2)				O2 Plasma	
	0	80	100	140	180	480	178	222	333	444	YES	NO
Kapton	✗0	✗0	✓1	✓1	✗0	✗0	✓1	✓1	✗0	✗0	✓1	✓1
Teflon	✗0	✗0	✓1	✓1	✗0	✗0	✗0	✓1	✗0	✗0	✓1	✗0
Silicon	✗0	✗0	✗0	✓1	✓1	✗0	✗0	✓1	✗0	✗0	✓1	✗0
PDMS	N/A	N/A	✓1	N/A	N/A	N/A	N/A		N/A	N/A	✓1	N/A

Figure 3-14: optimal range of thermal processing factors based on geometric analysis

- APTES treatment time: 100-140 minutes

- GO Concentration: ~ 200 µg/cm^2

- O$_2$ plasma: recommended

- Sonication time: <30 minutes (which is being processed)

64

Finally, after comparison of PR ratios considering the thermal processing factors, the following plot (Figure 3-15) shows that Kapton PDMS-186 have shown the best performance in comparison to other substrates. The performances were assessed based on comparing average PR ratio and average peel force. In this comparative study, the results of peel force and geometric analysis were utilized. The PDMS substrate was recently added to the experiments and is planned to be evaluated thoroughly in the future.
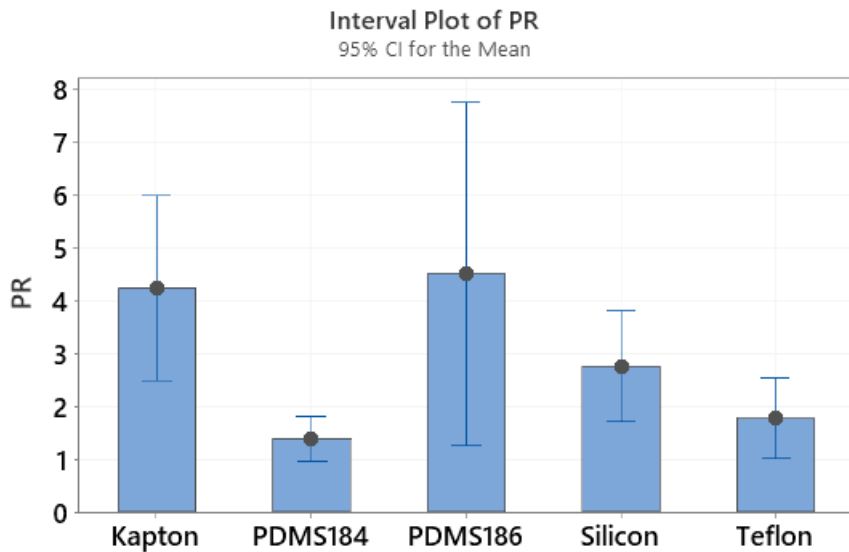
Figure 3-15: overall comparison of substrates based on geometric analysis of failure modes

3.4 Effects of thermal processing parameters on the bonding properties of the rGO-base samples

There are few parameters during the thermal processing of GO solution deposited on the substrates that significantly changes the mechanical properties of the rGO layers on the substrates. In this section the variation of bonding energies is analyzed based on factors of thermal processing of GO solution and determines whether each factor is significantly affects the bonding energies or not.

3.4.1 GO concentration

The concentration of the GO solution deposited on the substrate in anticipated to be the most significant parameter on the mechanical performance of the rGO layers. Obviously, the higher GO concentration leads to more layers of rGO on the samples which is corresponding to a lower bonding properties and better electrical conductivity of samples. Plots in Figure 3-16 illustrates that the cohesion energy of rGO layers reduces for higher concentration GO solution. The optimal value of 178 and 222 $\mu g/cm^2$ were obtained for Kapton and other substrates, respectively. Moreover, deposition on Kapton substrate leads to a much higher bonding energy of rGO layers versus other substrates.
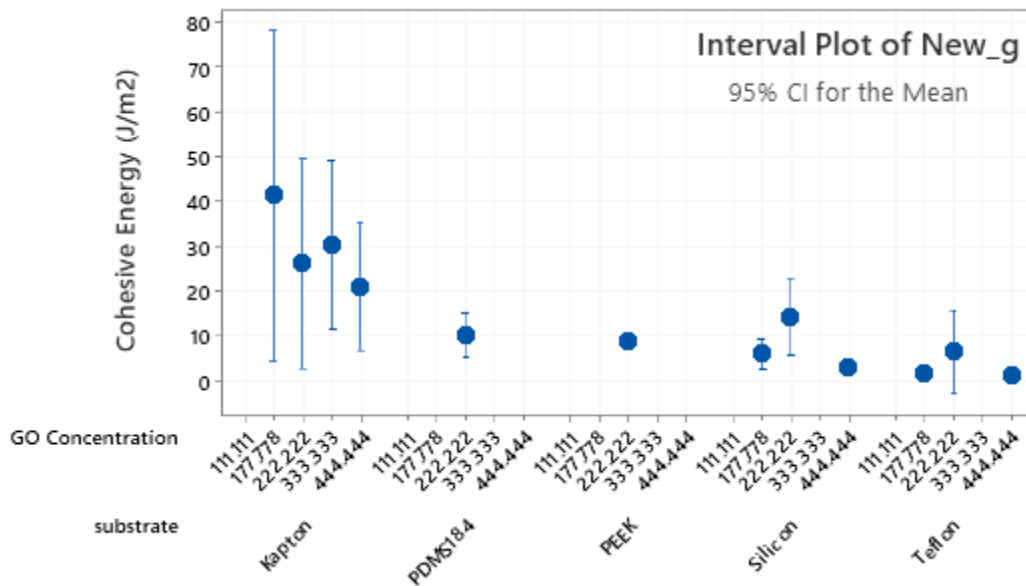
Figure 3-16: variation of cohesion energy versus GO concentration for all substrates

The variation of average adhesive energy versus concentration of GO solution is presented in Figure 3-17. The Kapton has shown the best overall adhesive energy in comparison to other

substrates, which is even more than Silicon. On the contrary with the cohesive energy, the GO concentration is not significant factor on the average adhesive energy.

Despite having low adhesive energy, the PDMS substrate showed a good cohesion energy that illustrate its potential to be served as a suitable candidate for next studies.
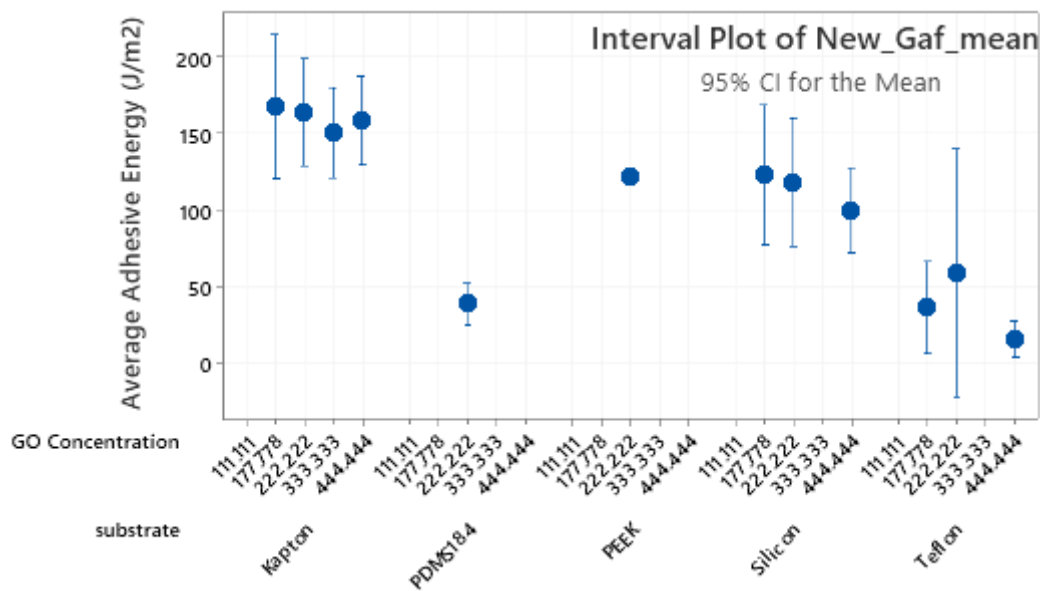
Figure 3-17: variation of cohesion energy versus GO concentration for all substrates

3.4.2   O₂ plasma surface treatment

As one of the most convenient method surface cleaning prior to bonding, the Oxygen (O_2) is used as gas for the plasma cleaning technology. The O_2 plasma is a convenient method for surface cleaning and wettability increasing of non-metal like polymers, glass, and other organic materials.

The mathematical model has confirmed the effectiveness of O_2 plasma treatment for substrate surface as shown in Figure 3-18 and Figure 3-19. Interestingly, the average adhesive

energy has shown significant variation versus O_2 plasma treatment while the cohesive energy was not affected by O_2 plasma significantly.
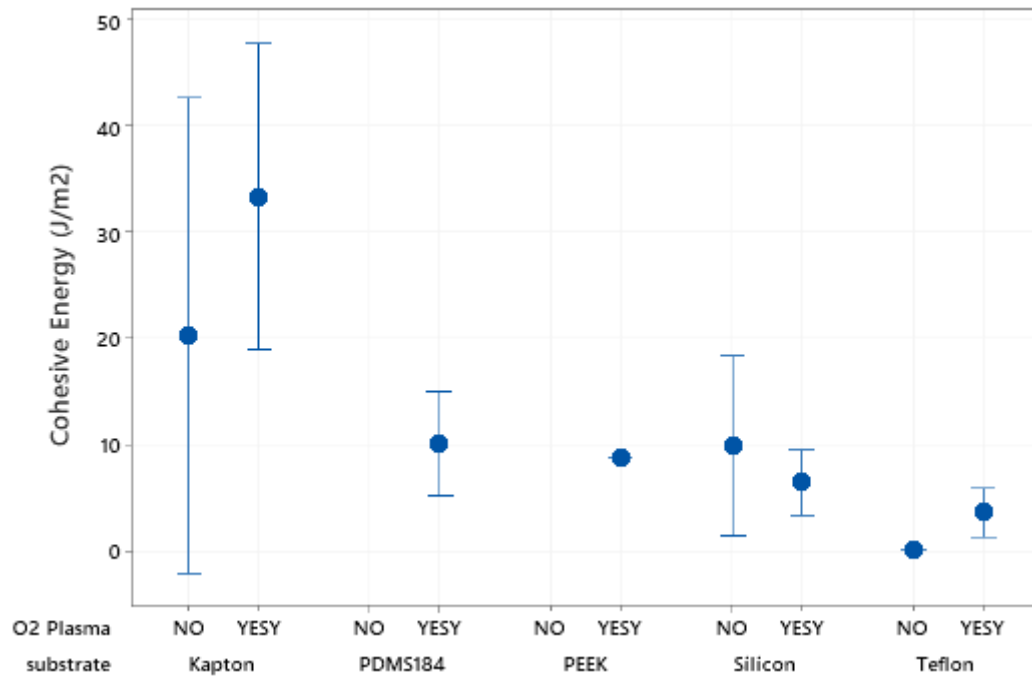
Figure 3-18: cohesive energy variation versus O_2 plasma treatment status for all substrates
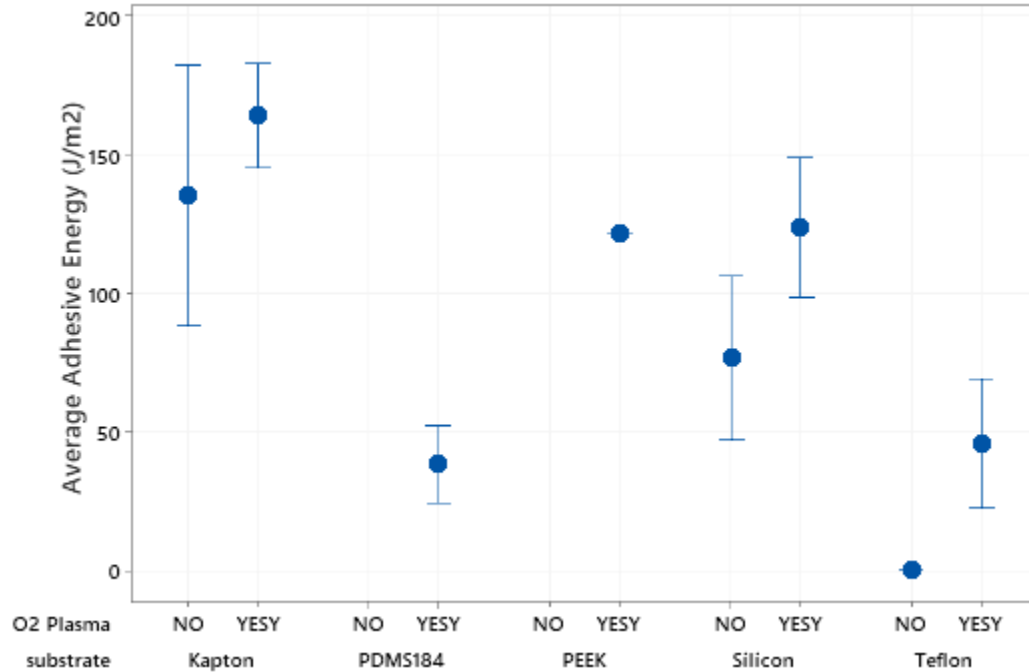
Figure 3-19: average adhesive energy variation versus O₂ plasma treatment status for all substrates

3.4.3   Surface treatment of GO

The surface treatment is a crucial factor on the bonding properties on the rGO layers on the substrate. The surface energy of the substrate changes significantly via surface treatment process. The APTES surface treatment is used before thermal reduction in this study. Considering the ANOVA results, the significance of APTES treatment is much less than the GO concentration such that it is significant by the confidence interval of 90%. As mentioned earlier in section 3.3, the APTES time of a range of 100~110 minutes was demonstrated as an optimal range.

3.4.4   Sonication time

The sonication treatment of the GO is a common step of GO solution preparation during the fabrication of the GO. The duration of sonication process significantly affects the mechanical properties of the rGO layers. Multiple sonication times were examined on Kapton substrate so that the lowest sonication time of 60 minutes was shown the best bonding energies as presented in Figure 3-20 and Figure 3-21. Therefore, for the rest of substrates, the sonication time of 50 minutes were set for experiments.
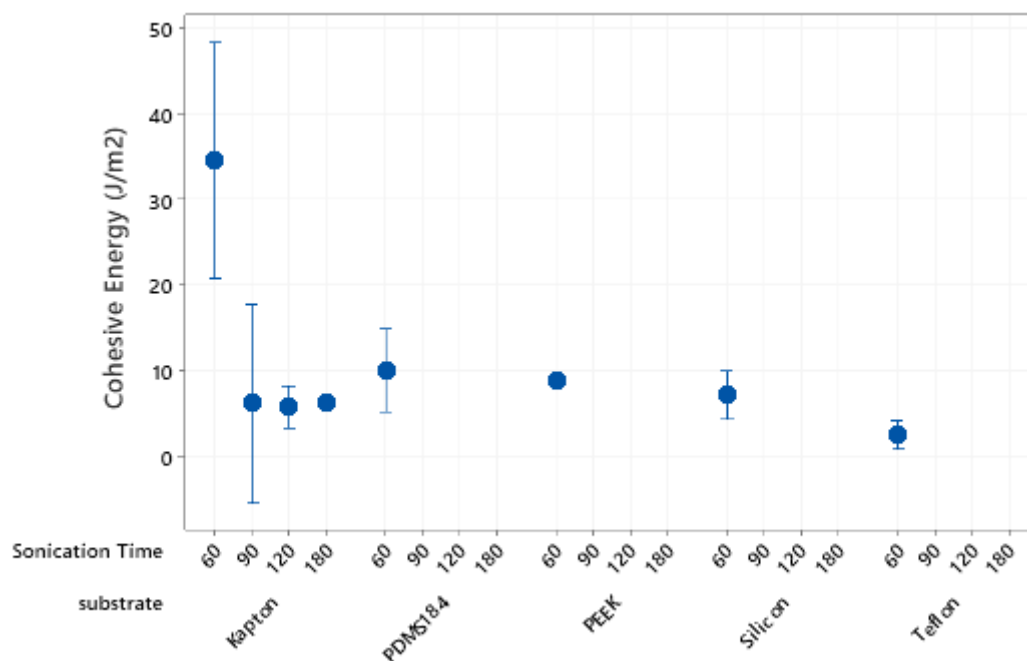
Figure 3-20: cohesive energy variation versus sonication time for all substrates
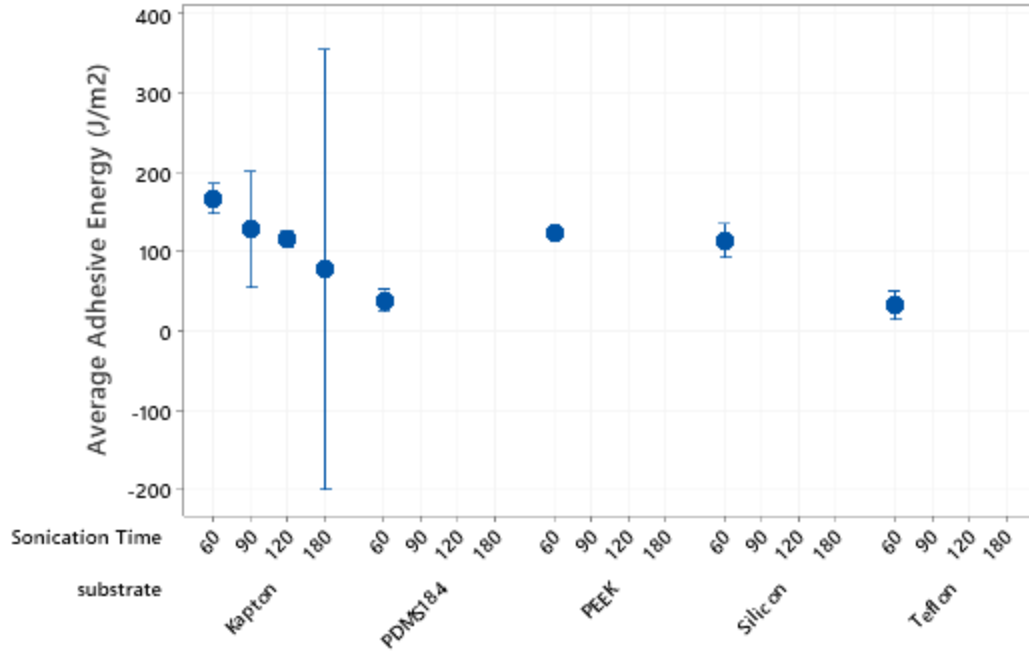
Figure 3-21: average adhesive energy variation versus sonication time for all substrates

3.5 Case studies

To demonstrate the effectiveness of mathematical model and geometric analysis on the bonding evaluation of the rGO samples, two cases studies are presented in this section. Each case study includes certain levels of thermal processing factors.

3.5.1 Case one

The first case of consideration contains the following factors' levels:

- APTES treatment time: 180 min.

- GO Concentration: 222 $\mu g/cm^2$

- O2 plasma: yes

- Sonication time: 60 minutes

71

Considering the plot in Figure 3-22, Kapton has shown the best adhesion energy for the case 1 as expected. For the rest of substrates, the cohesion energy is not statistically different demonstrating the good satisfactory performance Kapton substrate.
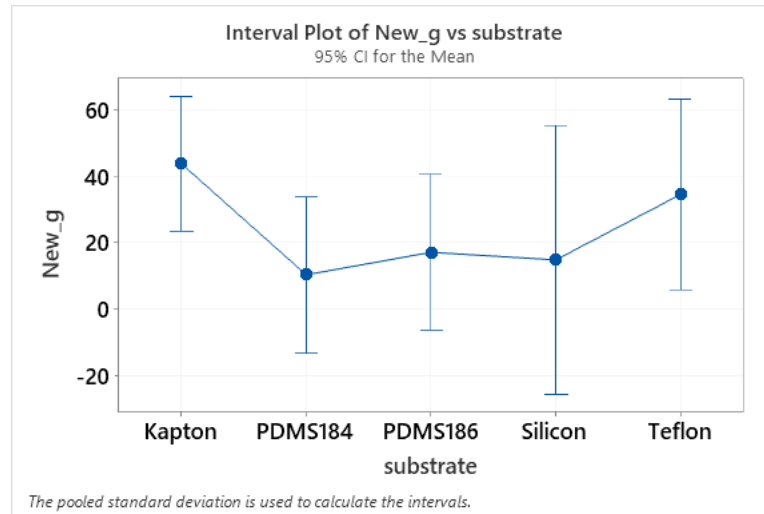
Figure 3-22: variation of cohesion energy for case 1

The adhesion energy has shown a different variation than cohesion energy (Figure 3-23). The Kapton has provided the highest adhesion energy and the PDMS showed the lowest adhesion energy.
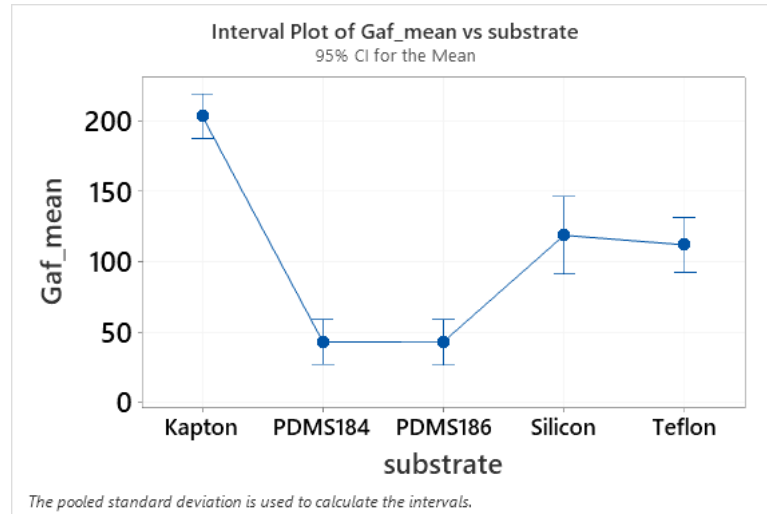
Figure 3-23: variation of adhesion energy for case 1

The performance ratio of substrates for the case 1 has shown two range of values (Figure 3-24). The first range with an average of PR=4 is for both Kapton and PDMS186 while the second range of about PR=1.75 was observed for the rest of substrates. As expected, the Kapton showed highest performance ratio. The PDMS substrate has shown completely different performance depending on its formulation such that the bonding energies of PDMS substrates are roughly same but the performance ratio of PDMS186 is much higher than PDMS184.
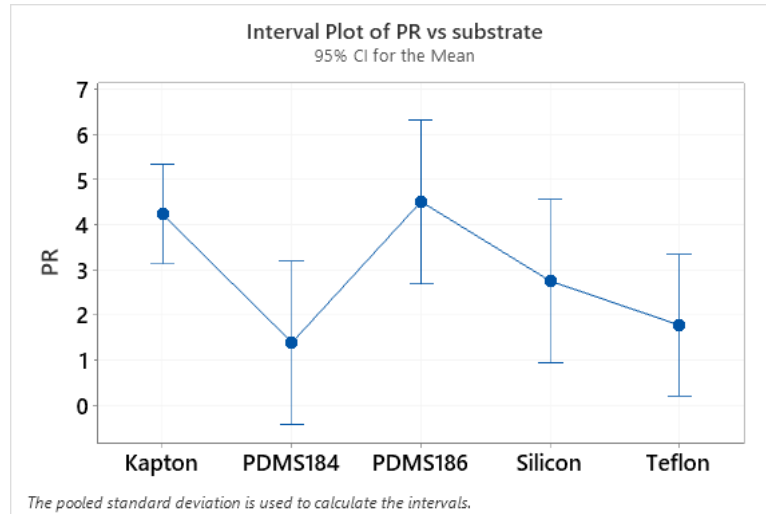
Figure 3-24: variation of performance ratio for case 1

3.5.2 Case two

The second case of consideration contains the following factors' levels:

- APTES treatment time: 180 min.

- GO Concentration: 178 μg/cm^2

- O2 plasma: yes

- Sonication time: 60 minutes

For this case of experimentation, the tests result is available for Kapton, Teflon, and Silicon substrates. Considering the plot in Figure 3-25, for this case, the cohesion energy is not statistically different for all substrates.
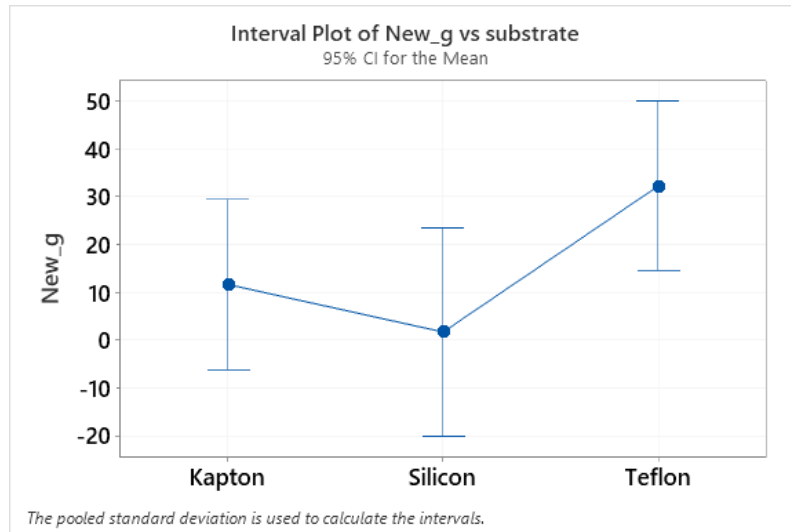
Figure 3-25: variation of cohesion energy for case 2

The adhesion energy has shown a different variation than cohesion energy (Figure 3-26). The Kapton has provided the highest adhesion energy. The performance ratio of substrates for the case 2 has shown the best value for the Teflon (Figure 3-27). Even thought, Kapton is the best candidate based on overall result so far, Teflon has shown better cohesion energy and performance in a specific factor like case 2.
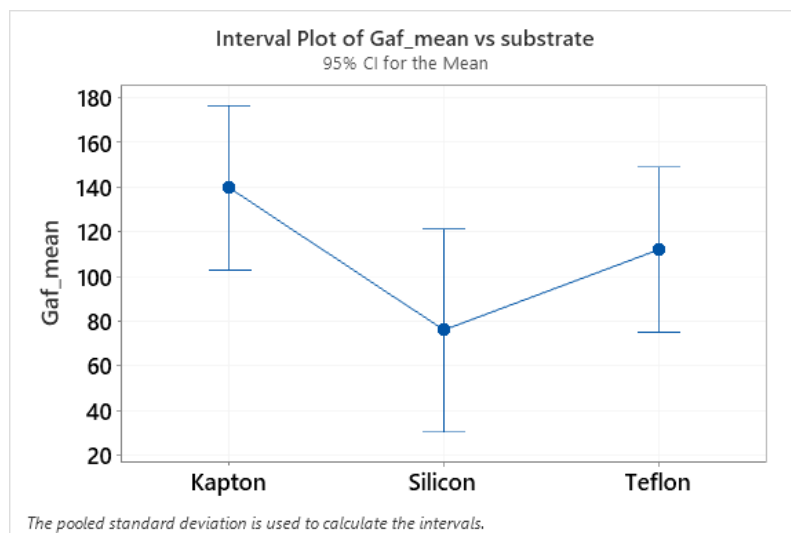
Figure 3-26: variation of adhesion energy for case 2

75
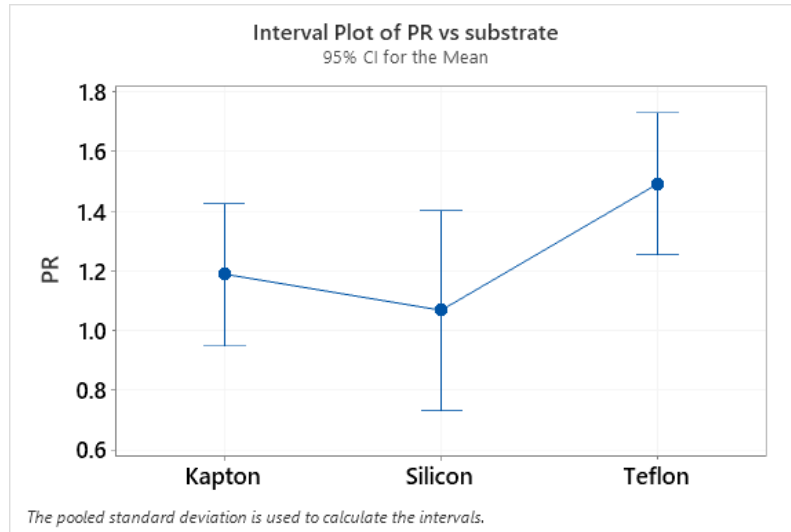
Figure 3-27: variation of performance ratio for case 2

3.6 Result summary

To summarize the results of experiments done based on multiple substrates and thermal processing factors, the Table 3-2 is provided. The followings substrates are listed in the table:

- Kapton

- Silicon

- Teflon

- PEEK

- PDMS

Considering the high number of thermal processing factors and their levels, and a much better performance of Kapton in initial sets of experiments in comparison to other substrates, the Kapton is the only substrate, which examined for all levels of thermal processing factors. After identifying the optimal levels of thermal processing factors, the experimentation for the

rest of substrates were done mostly focusing on the optimal levels. The optimal values of thermal processing factors were listed below based on Figure 3-14:

- O_2 plasma is required for all substrates.

    - Except silicon, other substrates have shown significant improvement of mechanical performance after O2 plasma treatment. It illustrates that the Silicon as a non-polymer substrate does not show improvement because of O_2 plasma treatment.

- ATPES treatment duration: the duration of between 100-140 minutes was shown the highest impact on the improving the bonding energies.

- Sonication time: for lowest examine time, which is 60 minutes, has illustrated the best mechanical performance. Since it was the lowest value, new sets of experimentation were designed for future studies to evaluate the impact of sonication times lower than 60 minutes on the bonding energies.

- GO concentration: considering noticeable difference of surface energy between Kapton and other substrates, the optimal value of GO concentration for Kapton is smaller than the rest of substrates. The optimal concentration of 178 μg/cm^2 was identified for Kapton whereas the 222 μg/cm^2 was determined for the rest of substrates.

Table 3-2: results summary for all experiments

Substrate	Result	O2 Plasma		APTES Duration (minute)						Sonication Time (minute)				GO Concentration (µg/cm²)			
		Yes	No	80	100	110	140	180	480	60	90	120	180	178	222	333	444
Kapton	Cohesion	33.25	20.20	2.969	54	65.9	17.62	19.51	98.666	34.54	6.152	5.69	6.1768	41.2	26	30.22	20.85
	Adhesion	164.19	135.2	140.5	175.1	135.1	161.4	155.5	170.79	166.31	128.05	115.73	77.6	167.6	163.8	150.6	158.6
	PR	3.088	1.27	0.9797	5.37	3.17	2.243	2.686	3.143	2.903	0.9948	3.09	0.9786	5.6	2.455	2.106	1.0197
	OCF	54.34	67.61	83.07	40.23	42.6	56.1	61.04	14.24	52.47	90.31	91.513	91.91	41.32	53.11	67.05	61.99
Silicon	Cohesion	6.38	9.86	14.55	3.658	2.909	4.67	4.98	13.44	7.11	-	-	-	5.83	14.2	-	2.281
	Adhesion	123.7	76.6	93.3	139.2	91.3	80	108.2	145.6	113.4	-	-	-	122.6	117.9	-	99.7
	PR	1.18	0.823	1.0232	0.9771	1.1989	0.663	1.58	1.1226	1.0923	-	-	-	1.0447	1.373	-	0.807
	OCF	80.22	58.66	80.09	80.67	77.69	58.2	75.4	78.76	74.83	-	-	-	76.65	69.6	-	78.78
Teflon	Cohesion	3.55	0	3.778	2.06	0	-	4.82	-	2.487	-	-	-	1.717	6.42	-	1.288
	Adhesion	45.8	0	61.3	28.7	0	-	47.4	-	32.04	-	-	-	35.7	58.6	-	15.13
	PR	1.14	1	0.9837	1.1865	1	-	1.256	-	1.1094	-	-	-	0.9683	1.356	-	0.9416
	OCF	76.34	58.91	81.62	76.46	58.91	-	70.94	-	72.32	-	-	-	77.04	59.46	-	83.67
PEEK	Cohesion	8.78	-	8.78	-	-	-	-	-	8.78	-	-	-	-	8.78	-	-
	Adhesion	121.92	-	121.92	-	-	-	-	-	121.92	-	-	-	-	121.92	-	-
	PR	0.9597	-	0.9579	-	-	-	-	-	0.9579	-	-	-	-	0.9579	-	-
	OCF	82.84	-	82.84	-	-	-	-	-	82.84	-	-	-	-	82.84	-	-
PDMS	Cohesion	10.05	-			-	-	10.05	-	10.05	-	-	-	-	10.05	-	-
	Adhesion	38.32	-			-	-	38.32	-	38.32	-	-	-	-	38.32	-	-
	PR	2.943	-			-	-	2.943	-	2.943	-	-	-	-	2.943	-	-
	OCF	48.4	-			-	-	48.4	-	48.4	-	-	-	-	48.4	-	-

Chapter 4: Conclusion and Future Works

4.1 Summary

In this study the mechanical strength and performance of rGO-based electronics were evaluated based on a new methodology of peel test. The rGO samples were fabricated on flexible polymeric substrates through thermal processing of GO solution. The followings are highlighted outcomes for this study:

- Considering the requirement of this study to conduct the peel force for nano-scale graphene-based layers on the flexible substrates and small-scale test samples, a new methodology was developed to measure the peel force consistently and repeatedly. This methodology is based on controlling the effective factors on the peel force such as peel rate, peel angle, application pressure and its timing, and timing between samples preparation and test start time. The coefficient of variation of this methodology was reported as 8% and 13% for within-laboratories and between-laboratories experiments, which dominantly lower than variation reported by ASTM by values of 37% and 70%.

- A semi-nonlinear mechanical model of peeling was developed to characterize the cohesive zone properties at the peel front.

- To distinguish between failure modes, a geometric analysis of remnant rGO particles on the tape back has been done. This analysis assesses the amounts of visible remnant rGO particles using an image processing technique to differentiate between cohesion and adhesion failure modes.

- As a result of geometric analysis, a parametric study was done to evaluate the mechanical performance of rGO samples.

- To connect the peel test and geometric analysis, a mathematical model was developed based on correlation between amount of remnant rGO particles and measured peel force. The mathematical model determines the interlayer cohesion failure energy and variation adhesive failure energy for each sample based on solving a system of linear equations. This model only requires conducting one test to determine the failure modes energies.

- After conducting the analyses mentioned above, it was demonstrated that the GO concentration, APTES treatment duration, and GO sonication time are the most significant factor of thermal processing, respectively.

- The Kapton has demonstrated the best performance and served as the best candidate for the fabricating rGO-based electronics based on thermal processing.

- Although the mechanical properties and surface energy of PDMS varies significantly by tis formulation, it shows high potential for being a suitable candidate for graphene-based electronics.

- Considering low surface energy of Teflon (PTFE), it would be viable candidate for transfer printing of graphene-based sensors. Despite the rGO layers showed very low adhesion boding to the Teflon substrate, the rGO layers on the Teflon had shown good uniformity itself.

4.2 **Future works**

Since the tape test is used in this study as the primary method for measuring the peel force, the limitation of associated with tape test is valid for this study. Employing other methods of bonding measurement may be helpful. On the other hand, this study focused on Kapton considering its best performance for several factors of thermal processing. This study could be extended to other substrates and introducing more failure modes through microscopic imaging. Followings are few suggestion for the future works:

- Improving the current mathematical model by adding more failure modes

  o requires conducting microscopic imaging

- Evaluation of bonding energy using bulge test (i.e., nano indentation test), which is a common method of characterizing of mechanical strength of nano-fabricated layers.

- Employing the shear lag theory to introduce the mode II or mixed modes of fracture into the computational model.

  o This method is based on measurement of strain mismatch between substrate and nanofabricated layers that looks an appropriate method for flexible substrates.

- Extending the experimentation on PDMS substrates as a good potential candidate.

- Examining the low sonication time impact on the bonding energies.

- Extending the work for electrical and chemical properties

Chapter 5: **References**

[1]   A. Dimiev, D. V. Kosynkin, A. Sinitskii, A. Slesarev, Z. Sun, J. M. Tour, *Science (80-.).* **2011**, *331*, 1168.

[2]   E. Kheirandish, M. Schofield, M. Gajdardziska-Josifovska, N. Kouklin, *Adv. Mater. Interfaces* **2020**, *7*, 2000561.

[3]   J. M. Garcia, R. He, M. P. Jiang, J. Yan, A. Pinczuk, Y. M. Zuev, K. S. Kim, P. Kim, K. Baldwin, K. W. West, L. N. Pfeiffer, *Solid State Commun.* **2010**, *150*, 809.

[4]   C. Zhao, L. Xing, J. Xiang, L. Cui, J. Jiao, H. Sai, Z. Li, F. Li, *Particuology* **2014**, *17*, 66.

[5]   A. Y. S. Eng, C. K. Chua, M. Pumera, *Electrochem. commun.* **2015**, *59*, 86.

[6]   C. Lee, X. Wei, J. W. Kysar, J. Hone, *Science (80-.).* **2008**, *321*, 385.

[7]   S. P. Koenig, N. G. Boddeti, M. L. Dunn, J. S. Bunch, *Nat. Nanotechnol.* **2011**, *6*, 543.

[8]   J. H. Kim, W. S. Chang, D. Kim, J. R. Yang, J. T. Han, G.-W. Lee, J. T. Kim, S. K. Seol, *Adv. Mater.* **2015**, *27*, 157.

[9]   S. Liu, T. H. Zeng, M. Hofmann, E. Burcombe, J. Wei, R. Jiang, J. Kong, Y. Chen, *ACS Nano* **2011**, *5*, 6971.

[10]   S. Kumar, A. Garg, A. Chowdhuri, *Mater. Res. Express* **2019**, *6*, 085620.

[11]   V. M. Pereira, A. H. Castro Neto, *Phys. Rev. Lett.* **2009**, *103*, DOI 10.1103/PhysRevLett.103.046801.

[12]   J. S. Bunch, S. S. Verbridge, J. S. Alden, A. M. Van Der Zande, J. M. Parpia, H. G. Craighead, P. L. McEuen, *Nano Lett.* **2008**, *8*, 2458.

[13]   Z. H. Aitken, R. Huang, *J. Appl. Phys.* **2010**, *107*, DOI 10.1063/1.3437642.

[14]   B. Chitara, L. S. Panchakarla, S. B. Krupanidhi, C. N. R. Rao, *Adv. Mater.* **2011**, *23*, 5419.

[15] X. Liu, M. C. Hersam, *Sci. Adv.* **2019**, *5*, DOI 10.1126/sciadv.aax6444.

[16] I. K. Moon, J. Lee, R. S. Ruoff, H. Lee, *Nat. Commun.* **2010**, *1*, DOI 10.1038/ncomms1067.

[17] J. Shen, Y. Hu, M. Shi, X. Lu, C. Qin, C. Li, M. Ye, *Chem. Mater.* **2009**, *21*, 3514.

[18] G. Eda, G. Fanchini, M. Chhowalla, *Nat. Nanotechnol.* **2008**, *3*, 270.

[19] G. Eda, M. Chhowalla, *Adv. Mater.* **2010**, *22*, 2392.

[20] M. C. Wang, S. Chun, R. S. Han, A. Ashraf, P. Kang, S. Nam, *Nano Lett.* **2015**, *15*, 1829.

[21] G. Guo, Y. Zhu, *J. Appl. Mech. Trans. ASME* **2015**, *82*, DOI 10.1115/1.4029635.

[22] S. R. Na, X. Wang, R. D. Piner, R. Huang, C. G. Willson, K. M. Liechti, *ACS Nano* **2016**, *10*, 9616.

[23] C. J. Brennan, J. Nguyen, E. T. Yu, N. Lu, *Adv. Mater. Interfaces* **2015**, *2*, 1500176.

[24] T. Jiang, R. Huang, Y. Zhu, *Adv. Funct. Mater.* **2014**, *24*, 396.

[25] L. Gong, I. A. Kinloch, R. J. Young, I. Riaz, R. Jalil, K. S. Novoselov, *Adv. Mater.* **2010**, *22*, 2694.

[26] A. Weerasinghe, C. T. Lu, D. Maroudas, A. Ramasubramaniam, *ACS Appl. Mater. Interfaces* **2017**, *9*, 23092.

[27] C. Xu, T. Xue, W. Qiu, Y. Kang, *ACS Appl. Mater. Interfaces* **2016**, *8*, 27099.

[28] M. S. Bronsgeest, N. Bendiab, S. Mathur, A. Kimouche, H. T. Johnson, J. Coraux, P. Pochet, *Nano Lett.* **2015**, *15*, 5098.

[29] G. Anagnostopoulos, C. Androulidakis, E. N. Koukaras, G. Tsoukleri, I. Polyzos, J. Parthenios, K. Papagelis, C. Galiotis, *ACS Appl. Mater. Interfaces* **2015**, *7*, 4216.

[30] M. Rezaee, L.-C. Tsai, M. I. Haider, A. Yazdi, E. Sanatizadeh, N. P. Salowitz, *Sci. Rep.* **2019**, *9*, 19805.

[31] L.-C. Tsai, M. Rezaee, M. I. Haider, A. Yazdi, N. P. Salowitz, in *ASME 2019 Conf. Smart Mater. Adapt. Struct. Intell. Syst.*, American Society Of Mechanical Engineers, **2019**.

[32] N. Padhye, D. M. Parks, A. H. Slocum, B. L. Trout, *Rev. Sci. Instrum.* **2016**, *87*, DOI 10.1063/1.4960172.

[33] M. Nase, M. Rennert, K. Naumenko, V. A. Eremeyev, *J. Mech. Phys. Solids* **2016**, *91*, 40.

[34] ASTM D3359 - 17, *Standard Test Methods for Rating Adhesion by Tape Test*, ASTM International, West Conshohocken, PA, 2017, **2017**.

[35] ASTM D4541-17, *Standard Test Method for Pull-Off Strength of Coatings Using Portable Adhesion*, ASTM International, West Conshohocken, PA, **2017**.

[36] ASTM D7234-19, *Standard Test Method for Pull-off Adhesion Strength of Coatings on Concrete Using Portable Pull-off Adhesion Testers*, ASTM International, West Conshohocken, PA, **2019**.

[37] ISO 4624, *Paints and Varnishes -- Pull-off Test for Adhesion*, Berlin, Germany, **2016**.

[38] ASTM D1002-10, *Standard Test Method for Apparent Shear Strength of Single-Lap-Joint Adhesively Bonded Metal Specimens by Tension Loading (Metal-to-Metal)*, ASTM International, West Conshohocken, PA, **2019**.

[39] ASTM D3163 - 01, *Standard Test Method for Determining Strength of Adhesively Bonded Rigid Plastic Lap-Shear Joints in Shear by Tension Loading*, ASTM International, West Conshohocken, PA, **2014**.

[40] ASTMD5868-01, *Standard Test Method for Lap Shear Adhesion for Fiber Reinforced Plastic (FRP) Bonding*, ASTM International, West Conshohocken, PA, **2014**.

[41] L. F. M. Da Silvaa, R. A. M. Da Silvaa, J. A. G. Chousala, A. M. G. Pintob, *J. Adhes. Sci.*

Technol. **2008**, *22*, 15.

[42] ASTM D1624 - 71, *Standard Specification for Acid Copper Chromate (Withdrawn 2006)*, ASTM International, West Conshohocken, PA, **2000**.

[43] ASTM D7249, *Standard Test Method for Facesheet Properties of Sandwich Constructions by Long Beam Flexure*, ASTM International, West Conshohocken, PA, **2020**.

[44] K. L. Mittal, *Progress in Adhesion and Adhesives*, **2015**.

[45] ASTM B571-97, *Standard Practice for Qualitative Adhesion Testing of Metallic Coatings 1*, ASTM International, West Conshohocken, PA, **2013**.

[46] J. Mikšovský, in *Int. Conf. Plasma Surf. Eng.*, **2012**.

[47] J. Tomastik, R. Ctvrtlik, *EPJ Web Conf.* **2013**, *48*, 00027.

[48] A. A. Volinsky, D. F. Bahr, M. D. Kriese, N. R. Moody, W. Gerberich, in *Compr. Struct. Integr.* (Eds.: I. Milne, I.. Ritchie, B. Karihaloo), Elsevier, **2003**, p. 5232.

[49] L. Tao, Z. Cao, P. Wang, R. S. Ruoff, W. Gao, D. Akinwande, J. W. Suk, R. Huang, K. M. Liechti, *Carbon N. Y.* **2013**, *69*, 390.

[50] Y.-W. Lu, P.-T. Lin, in *NSTI Nanotechnol. Conf. Trade Show*, **2007**, pp. 190–193.

[51] W.-S. Lei, K. Mittal, Z. Yu, in *Prog. Adhes. Adhes. II*, **2017**, pp. 351–380.

[52] ISO 14577-1, *Metallic Materials — Instrumented Indentation Test for Hardness and Materials Parameters — Part 1: Test Method*, **2015**.

[53] D. Allen, J. Wittge, A. Zlotos, E. Gorostegui-Colinas, J. Garagorri, P. J. McNally, A. N. Danilewsky, M. R. Elizalde, *Nucl. Instruments Methods Phys. Res. Sect. B Beam Interact. with Mater. Atoms* **2010**, *268*, 383.

[54] K. Kendall, *J. Phys. D. Appl. Phys.* **1975**, *8*, 1449.

[55] D. H. Kaelble, *Trans. Soc. Rheol.* **1960**, *4*, 45.

[56] A. N. Gent, G. R. Hamed, *J. Adhes.* **1975**, *7*, 91.

[57] S. C. L. Fischer, S. Boyadzhieva, R. Hensel, K. Kruttwig, E. Arzt, *J. Mech. Behav. Biomed. Mater.* **2018**, *80*, DOI 10.1016/j.jmbbm.2018.01.032.

[58] B. Mukherjee, R. C. Batra, D. A. Dillard, *Int. J. Solids Struct.* **2017**, *110–111*, DOI 10.1016/j.ijsolstr.2016.09.004.

[59] L. Afferrante, G. Carbone, *J. Mech. Phys. Solids* **2016**, *96*, DOI 10.1016/j.jmps.2016.07.013.

[60] C. Creton, M. Ciccotti, *Reports Prog. Phys.* **2016**, *79*, DOI 10.1088/0034-4885/79/4/046601.

[61] J. Chopin, R. Villey, D. Yarusso, E. Barthel, C. Creton, M. Ciccotti, *Macromolecules* **2018**, *51*, 8605.

[62] S. M. Xia, L. Ponson, G. Ravichandran, K. Bhattacharya, *J. Mech. Phys. Solids* **2015**, *83*, 88.

[63] R. Villey, P. P. Cortet, C. Creton, M. Ciccotti, *Int. J. Fract.* **2017**, *204*, 175.

[64] I. K. Mohammed, M. N. Charalambides, A. J. Kinloch, *J. Nonnewton. Fluid Mech.* **2015**, *222*, 141.

[65] C. Kovalchick, A. Molinari, G. Ravichandran, *J. Appl. Mech.* **2013**, *81*, 041016.

[66] Z. Peng, C. Wang, L. Chen, S. Chen, *Int. J. Solids Struct.* **2014**, *51*, 4596.

[67] K. L. Johnson, K. Kendall, A. D. Roberts, *Proceeding R. Soc. A* **1971**, *324*, 301.

[68] K. Kendall, *J. Adhes.* **1973**, *5*, 105.

[69] S. M. Xia, L. Ponson, G. Ravichandran, K. Bhattacharya, *J. Mech. Phys. Solids* **2013**, *61*,

838.

[70]   N. Wang, S. Xia, *J. Mech. Phys. Solids* **2017**, *98*, 87.

[71]   J. J. Bikerman, *J. Appl. Phys.* **1957**, *28*, 1484.

[72]   C. Jouwersma, *J. Polym. Sci. Part B Polym. Phys.* **1960**, *5*, 253.

[73]   S. Yurenka, *J. Appl. Polym. Sci.* **1962**, *6*, 136.

[74]   P. Rahulkumar, A. Jagota, S. J. Bennison, S. Saigal, *Int. J. Solids Struct.* **2000**, *37*, 1873.

[75]   I. K. Mohammed, M. N. Charalambides, A. J. Kinloch, *J. Nonnewton. Fluid Mech.* **2015**, *233*, 85.

[76]   T. Yang, K. M. Liechti, R. Huang, *J. Mech. Phys. Solids* **2020**, *145*, 104142.

[77]   M. Rezaee, L. Chih Tsai, A. Elyasigorji, M. Istiaque Haider, A. Yazdi, N. P. Salowitz, *Eng. Fract. Mech.* **2021**, *243*, 107525.

[78]   D. Das, I. Chasiotis, *J. Mech. Phys. Solids* **2020**, *140*, 103931.

[79]   S. Mousa, G. Y. Kim, *J. Mater. Process. Technol.* **2015**, *222*, 84.

[80]   P. Tran, T. D. Ngo, A. Ghazlan, D. Hui, *Compos. Part B Eng.* **2017**, *108*, 210.

[81]   J. Meza-Lopez, N. Noreña, C. Meza, C. Romanel, *J. Mater. Civ. Eng.* **2020**, *32*, 04020228.

[82]   S. M. Motevalizadeh, H. Rooholamini, *Theor. Appl. Fract. Mech.* **2021**, *112*, 102918.

[83]   B. Farahi, C. Cloutier, K. Sobolev, A. Faheem, M. Rezaee, C. Travis, in *Airf. Highw. Pavements*, **2021**.

[84]   D. S. Dugdale, *J. Mech. Phys. Solids* **1960**, *8*, 100.

[85]   H. B. Yin, L. H. Liang, Y. G. Wei, Z. L. Peng, S. H. Chen, *Int. J. Solids Struct.* **2020**, *191–192*, 473.

[86]   G. Alfano, *Compos. Sci. Technol.* **2006**, *66*, 723.

[87]   P. H. Geubelle, J. S. Baylor, *Compos. Part B Eng.* **1998**, *29*, 589.

[88]   H. D. Espinosa, P. D. Zavattieri, in *Mech. Mater.*, Elsevier, **2003**, pp. 333–364.

[89]   S. H. Song, G. H. Paulino, W. G. Buttlar, *Eng. Fract. Mech.* **2006**, *73*, 2829.

[90]   M. Alfano, F. Furgiuele, A. Leonardi, C. Maletta, G. H. Paulino, in *Int. J. Fract.*, Springer, **2009**, pp. 193–204.

[91]   X. Han, Y. Jin, L. F. M. da Silva, M. Costa, C. Wu, *J. Adhes.* **2020**, *96*, 490.

[92]   X. P. Xu, A. Needleman, *Model. Simul. Mater. Sci. Eng.* **1993**, *1*, 111.

[93]   M. J. van den Bosch, P. J. G. Schreurs, M. G. D. Geers, *Eng. Fract. Mech.* **2006**, *73*, 1220.

[94]   K. Kendall, *J. Adhes.* **1973**, *5*, 179.

[95]   A. D. Crocombe, R. D. Adams, *J. Adhes.* **1982**, *13*, 241.

[96]   D. H. Kaelble, *J. Adhes.* **1992**, *37*, 37.

[97]   Z. Peng, S. Chen, *Phys. Rev. E - Stat. Nonlinear, Soft Matter Phys.* **2015**, *91*, 1.

[98]   X. Feng, H. Cheng, A. M. Bowen, A. W. Carlson, R. G. Nuzzo, J. A. Rogers, *J. Appl. Mech.* **2013**, *80*, 061023.

[99]   M. Nase, B. Langer, W. Grellmann, *Polym. Test.* **2008**, *27*, 1017.

[100] I. K. Mohammed, A. J. Kinloch, M. N. Charalambides, *Procedia Struct. Integr.* **2016**, *2*, 326.

[101] A. Chiche, W. Zhang, C. M. Stafford, A. Karim, *Meas. Sci. Technol.* **2005**, *16*, 183.

[102] Z. L. Peng, S. H. Chen, A. K. Soh, *Int. J. Solids Struct.* **2010**, *47*, 1952.

[103] S. M. Xia, L. Ponson, G. Ravichandran, K. Bhattacharya, *Phys. Rev. Lett.* **2012**, *108*, 1.

[104] A. Ghareeb, A. Elbanna, *J. Appl. Mech.* **2019**, *86*, 071005.

[105] R. S. Rivlin, *Paint Technol.* **1944**, 215.

[106] Y. Sugizaki, T. Shiina, Y. Tanaka, A. Suzuki, *J. Adhes. Sci. Technol.* **2016**, *30*, 2637.

[107] Z. Peng, S. Chen, *Int. J. Solids Struct.* **2015**, *60*, 60.

[108] L. Avellar, T. Reese, K. Bhattacharya, G. Ravichandran, *J. Appl. Mech.* **2018**, *85*, 121005.

[109] G. C. Denolf, L. Haack, J. Holubka, A. Straccia, K. Blohowiak, C. Broadbent, K. R. Shull, *J. Polym. Sci. Part B Polym. Phys.* **2012**, *50*, 1706.

[110] ASTM D3359-09, *Standard Test Methods for Measuring Adhesion by Tape Test*, **2010**.

[111] B. N. J. Persson, A. Kovalev, M. Wasem, E. Gnecco, S. N. Gorb, *EPL (Europhysics Lett.* **2010**, *92*, 46001.

[112] T. J. Kwak, Y. G. Nam, M. A. Najera, S. W. Lee, J. R. Strickler, W.-J. Chang, *PLoS One* **2016**, *11*, e0166068.

[113] I. S. Park, T. J. Kwak, G. Lee, M. Son, J. W. Choi, S. Choi, K. Nam, S. Y. Lee, W. J. Chang, K. Eom, D. S. Yoon, S. Lee, R. Bashir, S. W. Lee, *ACS Nano* **2016**, *10*, 4011.

[114] L. A. Kulakov, M. B. McAlister, K. L. Ogden, M. J. Larkin, J. F. O'Hanlon, *Appl. Environ. Microbiol.* **2002**, DOI 10.1128/AEM.68.4.1548-1555.2002.

[115] T. J. Kwak, W. Kwon, J. Yang, S. W. Lee, W. J. Chang, *Anal. Methods* **2018**, *10*, 4648.

[116] C. Parmer, "Cole Parmer Ultrasonic Bath M-Series Operating Manual," can be found under https://pim-resources.coleparmer.com/instruction-manual/08895-xx.pdf, **n.d.**

[117] M. Rezaee, L.-C. Tsai, A. Elyasigorji, M. I. Haider, A. Yazdi, N. P. Salowitz, *Eng. Fract. Mech.* **2021**, *243*, 107525.

[118] G. Wang, Z. Dai, J. Xiao, S. Feng, C. Weng, L. Liu, Z. Xu, R. Huang, Z. Zhang, *Phys. Rev. Lett.* **2019**, *123*, DOI 10.1103/PhysRevLett.123.116101.

Chapter 6: **Curriculum Vitae**

EDUCATION
Graduate
Ph.D. in Structural Health Monitoring (2021)

College of Engineering and Applied Sciences, University of Wisconsin-Milwaukee, Milwaukee, WI, US

Minor: Mechanics *(relevant courses: Sensing in Structures and Intelligent Materials, Design for Reliability, Design for Six Sigma (DFSS), Reduced Order Modeling, Design of Experiments (DOE), and Algorithm Design & Analysis)*

Dissertation: Evaluation of mechanical robustness of GO-based electronics using controlled peel test and image processing

Advisor: Nathan Salowitz

M.A in Structural Engineering (2007)

Shahrood University of Technology (SUT), Shahrood, Iran

Dissertation: Shape Optimization of Shell Structures Using Mathematical Programming

Undergraduate
B.A in Civil Engineering (2003)

Mazandaran University (MU), Babol, Mazandaran, Iran

RESEARCH EXPERIENCE
1. *University of Wisconsin-Milwaukee, Advanced Structures Laboratory*

Title:	Research Assistant (Sep. 2017 – now)
Supervisor:	Prof. Nathan Salowitz
Project:	Customized Inkjet Printing of Graphene-Based Real-time Water Sensors
Funded by:	National Science Foundation (NSF), Grant # 1727846
Collaborators:	Prof. Mark Hersam

- Walter P. Murphy Professor of Materials Science and Engineering and Director of the Materials Research Center at Northwestern University
- Founder & President of Volexion

   Prof. Junhong Chen;
- Professor of Molecular Engineering at Pritzker School of Molecular Engineering, University of Chicago
- lead water strategist at Argonne National Laboratory, IL
- former program director for the Engineering Research Centers (ERC) program of the U.S. National Science Foundation (NSF)

Application:	a real-time qualification of water at homes without any required skill for costumers
Duties:	Development of a new method for bonding evaluation of micro/nano-fabricated devices on flexible substrates; Prototyping a peel test method for thin and flexible substrates, high precision measurement device setup, identifying sensitive factors on nano-scale thick electronics robustness, design and manufacturing the test fixture, conducting tests on prepared samples and data collecting, post-processing of tests result, image processing, developing mathematical model to characterize bonding strength of Nano-fabricated Graphene-based devices

2. *University of Wisconsin-Milwaukee*

Title:	Conducting Structural Simulation (July 2020- now)
Supervisor:	Prof. Konstantin Sobolev
Project:	Auxetic concrete structures

| Application: | resilience and maintenance of concrete bridges |
| Duties: | design the pattern and conduct the simulations of Auxetic concrete structure |

3. *University of Wisconsin-Milwaukee*

Title:	Co-author in writing of "Introduction to Structural Design" book (Sep. 2017 – now)
Supervisor:	Prof. Habib Tabatabai
Application:	in the course of "Introduction to Structural Design"; the first book on elementary structural design concepts for undergraduate students (up to writers' knowledge)
Duties:	Preparing materials for book, drawing the images (using AutoCAD and Inventor software), designing the tables and appendices, typing and editing the context.

4. *University of Wisconsin-Milwaukee, Structural Laboratory*

Title:	Volunteer Research Assistant (Jun. 2016 – Sep. 2017)
Supervisor:	Prof. Al Ghorbanpoor
Project:	Corrosion detection in prestressed concrete girders using magnetic flux leakage
Funded by:	Federal Department of Transportation (DOT). The final product of this project, which is a pending patent now, was sold to federal DOT
Application:	lifetime maintenance of existing bridges and other reinforced concrete members
Duties:	ANSYS simulation of magnetic flux leakage (MFL) phenomenon to illustrate the capability of MFL in characterization of corrosions, 3D transient electro-magnetic simulation, post-processing of simulations to propose the tabulated data as an efficient tool for corrosion geometric properties.

WORK EXPERIENCE
- *Sr. Mechanical Engineer*, (Mar. 2021- Present)

  Zoomlion Heavy Industry NA, Inc.
  Yorkville, Wisconsin, United States
- *Research & Teaching Assistant*, (Sep 2017- May 2021)

  University of Wisconsin-Milwaukee
  Milwaukee, Wisconsin, United States

ACADEMIC PROFILES
- Google scholar , ORCiD , Publon

In-PROCESS PUBLICATIONS
- **Maysam Rezaee,** Nathan Picchietti Salowitz. "Semi-Nonlinear analytical model for peel tests to identify the actual cohesive zone length", < under revision>, *Engineering Failure Analysis*
- Azam Elyasigorji, **Maysam Rezaee,** Al Ghorbanpoor. "A correlation-based 3D analysis of MFL signals to characterize the corroded regions in Pre-stressed concrete girders", <submitted Feb. 2021>, *NDT & E International*

PUBLISHED JOURNAL PAPERS
- **Rezaee, Maysam**, Li-Chih Tsai, Azam Elyasigorji, Muhammad Istiaque Haider, Armin Yazdi, and Nathan P. Salowitz. "Quantification of the mechanical strength of thermally reduced graphene oxide layers on flexible substrates." *Engineering Fracture Mechanics* 243 (2021): 107525. (https://doi.org/10.1016/j.engfracmech.2021.107525)
- **Maysam Rezaee,** Li-Chih Tsai, Muhammad Istiaque Haider, Armin Yazdi, Ehsan Sanatizadeh, Nathan Picchietti Salowitz. "Quantitative peel test for thin films/layers based on a coupled parametric and statistical study", *Scientific Reports (Nature),* 9.1 (2019): 1-11

(https://doi.org/10.1038/s41598-019-55355-9)
- Haider, Muhammad Istiaque, **Maysam Rezaee**, Armin Yazdi, and Nathan Picchietti Salowitz. "Investigation into post constrained recovery properties of nickel-titanium shape memory alloys." *Smart Materials and Structures* (2019).
  (https://doi.org/10.1088/1361-665X/ab3ad4)
- F. Elyasigorji, **M. Rezaee**, A. Elyasigorji, "Influence of Persian Garden as Urban Green Spaces on Promotion of Social Interactions Citizens; Case Study: Garden Chehel Sotun (Mellat Park) of Behshahr City", *Journal of Civil Engineering and Urbanism (JCEU)*, 2014

PUBLISHED CONFERENCE PAPERS
- Elyasigorji, **M. Rezaee,** A. Ghorbanpoor; "Characterization of Corrosion in PS Concrete Girders by Correlation Analysis", *The ASCE Structural Congress,* Saint Louis, MI, US, 2020. *(peer-reviewed)*
  (https://doi.org/10.1061/9780784482650.018)
- Li-Chih Tsai, **Maysam Rezaee**, Muhammad Istiaque Haider, Armin Yazdi, Nathan Salowitz. "Quantitative Measurement of Thin Film Adhesion Force", *The ASME 2019 Conference on Smart Materials, Adaptive Structures and Intelligent Systems,* Louisville, KY, US, 2019. *(peer-reviewed)*
  (https://doi.org/10.1115/SMASIS2019-5615)
- Muhammad Istiaque Haider, **Maysam Rezaee**, Li-Chih Tsai, Nathan Salowitz. "Mechanics of Post Constrained Recovery Residual Stress Produced by NiTi", *The ASME 2019 Conference on Smart Materials, Adaptive Structures and Intelligent Systems,* Louisville, KY, US, 2019. *(peer-reviewed)*
- (https://doi.org/10.1115/SMASIS2019-5619)
- A. Elyasigorji, **M. Rezaee**, A. Ghorbanpoor; "Magnetic Corrosion Detection in Concrete Structures", *The ASCE 2019 International Conference on Sustainable Infrastructure,* Los Angeles, CA, US, 2019. *(peer-reviewed)*

  (https://doi.org/10.1061/9780784482896.027)
- **M. Rezaee**, A. Elyasigorji, F. Elyasigorji, "Analytical Evaluation of Inter-Story Beam Effects on Lateral Stiffness of Moment Frames", *10th International Congress on Civil Engineering*, Tabriz, Iran, May 2015
- A. Elyasigorji, **M. Rezaee**, "The Assessment of Eigenvalues Using New Graph and Laplacian Matrix of Form II", *International Conf. on Civil Engineering Architecture & Urban Sustainable Development,* Tabriz, Iran, (2013) <Persian>

PAPER REVIEWS DONE for
- Journal of Structural Health Monitoring (Sage Publications) – 2 paper reviews; *visible on Publon*
- Journal of Sock and Vibration (Hindawi Publications) – 1 paper review
- Journal of IEEE Transaction on Industrial Electronics (Sage Publications) – 1 paper review; *visible on Publon*
- The ASME 2020 Conference on Smart Materials, Adaptive Structures and Intelligent Systems, SMASIS 2020, (ASME Publications), 4 paper reviews
- The Transportation Research Board (TRB), Standing Committee on Construction of Bridges and Structures (AKC40), 1 paper review

PRESENTATIONS
- Madison Mechanical Symposium 2019: University of Wisconsin-Madison (Mar. 2019)
  - *Quantitative Evaluation of Bonding Strength of Thin Films*
- ASCE International Conference on Sustainable Infrastructure; Los Angele, CA, (Nov. 2019)
  - *Magnetic Corrosion Detection in Concrete Structures*
- ASCE Structural Congress; Saint Louis, MI, (April 2020)
  - *Characterization of Corrosion in PS Concrete Girders by Correlation Analysis*
- Invited Speaker for "Mechanics Seminar"; University of Wisconsin-Milwaukee, WI, (Feb. 2020)
  - *Direct measurement of nano-layer cohesion energy using peel test*

WORK EXPERIENCE in IRAN
- *CEO* of "Structure Time Energy" Consulting Engineering Co., (2014-2016)

- *Certificate of Employment as Supervisor and Designer Engineer*: Was Licensed by Ministry of Road, Housing and Urban and Construction Engineering Disciplinary Organization with Grade 1/3 (Perfect Experience) in the National Engineering Entrance Exam (2010-2016)
- As *Controller and Inspector*: For Buildings of Behshahr (Both Design and Supervision) (2009- 2012)
- As *Designer and Supervisor*: For Buildings Over 20000 m2 (2007- Present) *
- *Construction Director*: Miarkola Residential Complex (502-units, Approximately 50000m^2 Area) and Behshahr Residential Complex (60-units, Approximately 5500m^2 Area), (2010-2012)
- *Structural design*: Steel Framed Flour Factory with Area Approximately 4000 m2 and Cooperation with Buhler Co., Neka, Mazandaran, Iran (2010) *
- *Designer and Supervisor*: For Rural Buildings of Behshahr, Appointed by Government (2010) *
- *Architectural and Structural Design and supervision*: For 8-Story, Steel Framed Structure with Area Approximately 2500 m2 Which Was Introduced as distinguished Maskan Mehr Building, by Governor of Mazandaran Province, Rostamkola, Behshahr, Mazandaran, Iran (2009) *
- As *Designer*: In Arvin Bana Consulting Engineering Co. (2008) *
- *Full Surveying* in 5 Villages for Issuance of Property Deed for Over 2000 units. (2003-2004)

*Structural Designs Have Been Calculated Using ETABS, **SAFE**, and **SAP2000** Software
*Architectural Designs Have Been Designed Using **AutoCAD**, **Autodesk Revit** Software

TEACHING EXPERIENCE

Teaching assistant, University of Wisconsin-Milwaukee**, (Fall 2017 & Spring 2020)
- Courses:
  - Dynamic
  - Design of Machine Elements
- Departments: Civil & Environmental Engineering, Mechanical Engineering

Instructor, University College of Komeil**, Iran,** (2012-2016)
- Courses:
  - Structural Design (Concrete & Steel)
  - Structural Analysis
  - Strength of Materials
  - Computer-Based Engineering Analysis and Design
  - Statics
  - Soil Mechanics
- Department of Civil Engineering

Instructor, Golestan University**, Iran,** (2012-2014)
- Courses:
  - Structural Design (Concrete & Steel)
  - Structural Analysis
  - Concrete Technology
  - Open Channels Hydraulics
- Department of Civil Engineering

Teaching Assistant, Noshirvani University of Technology**, Iran,** (2008-2009)
- Courses:
  - Structural Analysis
- Department of Civil Engineering

SKILLS & SOFTWARE PACKAGES
- Programming
  - Python (basic)
  - MATLAB, FORTRAN (advanced)

- Simulation software
  - ABAQUS, ANSYS (advanced)
- Structural Design software
  - SAP2000, ETABS, SAFE (advanced)
- Computer Science
  - Data Structures
  - Algorithm design & Analysis
- Statistical Analysis software
  - Minitab (advanced)
  - Relisoft (basic)
- Modeling software
  - AutoCAD, Inventor, Revit (advanced)
  - Solidworks, CATIA (basic)
- Drafting software
  - Microsoft Office (Word, Excel, and PowerPoint) (advanced)
  - LaTeX (basic)

AWARDS AND HONORS
- 4-year tuition waiver award for bachelor's degree, (February 2003)
- 3-year tuition waiver award for master's degree, (August 2007)
- Top student among graduate students in the class of 2007 in the department of Structural Engineering at the Shahrood University of Technology
- Winner of Student Poster Competition, University of Wisconsin-Milwaukee, (2017)
- Chancellor's Graduate Student Award at UWM, (Spring 2018, 2020)
- UWM Graduate School Travel Grant (2019)

ASSISTANTSHIP RECIPIENT FOR
- Research Assistant in Department of Mechanical Engineering
  - Fall 2017
  - Spring & Fall 2018
  - Spring & Fall 2019
- Teaching Assistant in Department of Mechanical Engineering
  - Fall 2017
  - Spring & Fall 2020

PROFESSIONAL MEMBERSHIP
- American Society of Civil Engineers (ASCE)
- American Society of Mechanical Engineers (ASME)
- American Institute of Steel Construction (AISC)
- Vice- President Structural Engineering Society at UWM
- Member of the Society of Women Engineers at UWM (SWE) (2015-present)
- Member of the Construction Firm (Firm Title: Arshad Niyaresh Sazeh (ANS), Iran, Mazandaran Province (Fall 2010- present)
- Member of the "Construction Engineering Organization" of Mazandaran Province and Iran (2007- Present)
- Member of the "Construction Engineering Association" of Behshahr City (2007- Present)
- Commission Member of Education in the "Construction Engineering Association" of Behshahr (2010- 2014)